

See discussions, stats, and author profiles for this publication at: <https://www.researchgate.net/publication/232740207>

Controlling Electronic Product Branching at Conical Intersections in the UV Photolysis of Para-Substituted Thiophenols.

ARTICLE *in* THE JOURNAL OF PHYSICAL CHEMISTRY A · OCTOBER 2012

Impact Factor: 2.69 · DOI: 10.1021/jp308804d · Source: PubMed

CITATIONS

15

READS

15

5 AUTHORS, INCLUDING:



Tom Oliver

University of Bristol

39 PUBLICATIONS 634 CITATIONS

SEE PROFILE



Graeme King

VU University Amsterdam

22 PUBLICATIONS 448 CITATIONS

SEE PROFILE

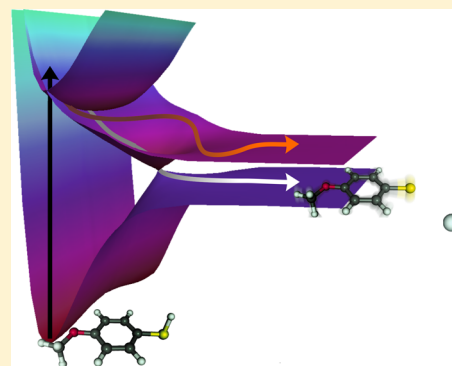
Controlling Electronic Product Branching at Conical Intersections in the UV Photolysis of *para*-Substituted Thiophenols

Thomas A. A. Oliver,[†] Graeme A. King,[‡] David P. Tew, Richard N. Dixon, and Michael N. R. Ashfold*

School of Chemistry, University of Bristol, Bristol BS8 1TS, United Kingdom

S Supporting Information

ABSTRACT: H (Rydberg) atom photofragment translation spectroscopy and high-level ab initio electronic structure calculations are used to explore the photodissociation dynamics of three *para*-substituted thiophenols (*p*-YPhSH; Y = CH₃, F, and MeO). UV excitation in the wavelength range 305 > λ_{phot} > 240 nm results in S–H bond fission and formation of *p*-YPhS radicals in their ground (\tilde{X}^2B_1) and first excited (\tilde{A}^2B_2) electronic states; the \tilde{X}/\tilde{A} state product branching ratio, Γ , varies with *para*-Y substituent and excitation wavelength. Excitation at $\lambda_{\text{phot}} < 265$ nm results in direct population of the dissociative $1^1\pi\sigma^*$ potential energy surface (PES). Γ falls across the series *p*-CH₃PhSH > *p*-FPhSH > *p*-MeOPhSH. Branching is ultimately determined at the conical intersection (CI) formed by the $1^1\pi\sigma^*$ and ground (S_0) PESs at extended $R_{\text{S-H}}$ bond length but is sensitively dependent on the orientation of the S–H bond (relative to the ring plane) in the S_0 molecules prior to photoexcitation. Excitation at $\lambda_{\text{phot}} > 265$ nm populates quasi-bound levels of the respective $1^1\pi\pi^*$ states, which predissociate rapidly by tunneling under the lower diabats of the $1^1\pi\pi^*/1^1\pi\sigma^*$ CI at short $R_{\text{S-H}}$. Less extreme \tilde{X}/\tilde{A} product branching ratios are measured, implicating intramolecular vibrational redistribution within the photoexcited $1^1\pi\pi^*$ molecules prior to their sampling the region of the $1^1\pi\sigma^*/S_0$ CI.



1. INTRODUCTION

Dissociation on a $1^1\pi\sigma^*$ excited state potential energy surface (PES) is now widely recognized as a competitive nonradiative decay mechanism in molecules like phenols and azoles, chromophores that are the building blocks of certain DNA bases and aromatic amino-acids.^{1,2} The $\pi\sigma^*$ excited state is formed by $\sigma^* \leftarrow \pi$ electron promotion and is repulsive with respect to the X–H stretch coordinate (where the heteroatom, X = N, O, S, etc.). The UV absorption spectra of such heteroaromatic molecules are typically dominated by $\pi^* \leftarrow \pi$ excitations that constitute $1^1\pi\pi^*$ states. There are two ways in which a $1^1\pi\sigma^*$ state can be populated. Initial photoexcitation of isoenergetic $1^1\pi\pi^*$ levels can, by nonadiabatic coupling at conical intersections (CIs), result in population transfer to $1^1\pi\sigma^*$ states. Alternatively, the $1^1\pi\sigma^*$ state can be directly photoexcited, despite the typically low oscillator strength of the $\sigma^* \leftarrow \pi$ transition. Once the $1^1\pi\sigma^*$ PES is populated, the nuclei experience gradients that encourage X–H bond extension and thus the impetus for prompt X–H bond fission.

The near UV photolysis of thiophenol (PhSH) and substituted thiophenols has been the focus of many experimental studies over the last six years, in the gas^{3–8} and solution^{9–11} phases. The prevailing consensus is that S–H bond fission, *via* the lowest $1^1\pi\sigma^*$ state, is the dominant relaxation pathway over a large range of excitation wavelengths. Excited state S–H bond cleavage produces translationally fast H atoms and thiophenoxy (PhS) radicals. The latter are formed in a limited range of vibrational states, in both their ground (\tilde{X}^2B_1) and first excited (\tilde{A}^2B_2) electronic states. These

observations contrast with the documented excited state dynamics of phenol (PhOH), wherein excitation at long UV wavelengths populates $1^1\pi\pi^*$ levels that can predissociate by coupling to the $1^1\pi\sigma^*$ PES, but the quantum yield for O–H bond fission (cf., S–H bond fission in PhSH) is considerably smaller. Irrespective of the excitation wavelength, however, the dominant photoproduct following O–H bond scission is a ground state phenoxyl (\tilde{X}^2B_1) radical (plus an H atom).^{7,12,13}

Devine et al. studied the photodissociation dynamics of bare PhSH at many photolysis wavelengths (λ_{phot}) and determined values for the S–H bond strength and the energy splitting between the \tilde{X} and \tilde{A} states of the PhS radical, $\Delta E(\tilde{A} - \tilde{X})$.⁶ The electronic structure of these two states differs by the localization of the singly occupied molecular orbital (SOMO). The SOMO of the ground state PhS radical is localized over the mixed sulfur 3p_x–benzene π (b_1) orbital, whereas the SOMO in the \tilde{A} state comprises purely the sulfur 3p_y (b_2) lone pair.³ The similar vibrational energy disposal in the \tilde{X} and \tilde{A} state radical products was understood to reflect late branching in the dissociation coordinate, induced by bifurcation at the CI between the $1^1\pi\sigma^*$ and ground (S_0) state PESs; see Figure 1.^{6,7,9} The precise mechanism by which the S–H bond breaks, the way this varies with excitation wavelength, and the specific nuclear motions that couple the relevant PESs have, however, all proved more elusive.

Received: September 5, 2012

Revised: October 25, 2012

Published: October 30, 2012

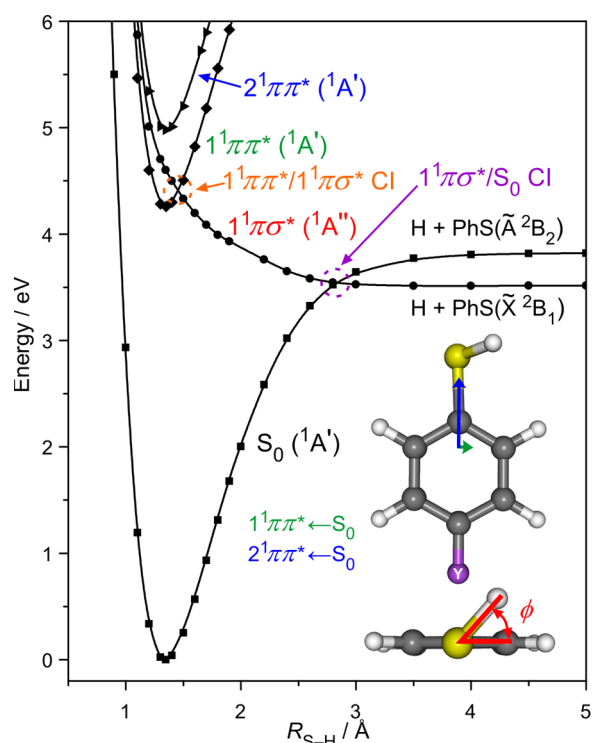


Figure 1. Relaxed PECs calculated at the CASPT2(10/10)/aug(S)-cc-pVTZ level for the S_0 , $1^1\pi\pi^*$, $1^1\pi\sigma^*$, and $2^1\pi\pi^*$ states of PhSH as a function of R_{S-H} . The dihedral angle, ϕ , that the S–H bond makes with the benzene ring is depicted in red in the lower representation of the molecule. The $1^1\pi\pi^* \leftarrow S_0$ and $2^1\pi\pi^* \leftarrow S_0$ parent transition dipole moments (TDMs) for PhSH are superimposed on the skeletal structure, the $1^1\pi\sigma^* \leftarrow S_0$ TDM lies perpendicular to the ring plane and is not shown.

The ion-imaging study of Lim et al. demonstrated (albeit only at $\lambda_{\text{phot}} = 243.1$ nm) that the electronic branching between the \tilde{X} and \tilde{A} state PhS products resulting from photolysis of PhSD was sensitive to *para* (*p*)-Y substitution (for Y = H, fluoro (F), and methoxy (MeO)).⁵ Prior density functional theory (DFT) calculations, for a similar set of *p*-substituted thiophenols, suggested that the minimum energy ground state configurations did not necessarily involve the S–H(D) bond lying in the plane defined by the benzene ring but, rather, at a dihedral angle ϕ , as shown in Figure 1.¹⁴ DFT/B3LYP calculations by Lim et al. predicted minimum energy geometries with $\phi = 0, 31$, and 73° , respectively, for Y = H, F, and MeO.⁵ From time-dependent (TD)-DFT calculations, Lim et al.⁵ concluded that the torsional barrier (and thus the driving force toward planarity) on the $1^1\pi\sigma^*$ state PES was similar for each thiophenol. They also anticipated significant activity in the torsional mode, $\tau_{\text{SH(D)}}$, in the case of dissociating molecules where the S_0 minimum energy geometry involved ϕ far from 0° . Lim et al. rationalized that, if such motion was not damped by the time a dissociating molecule reached the $1^1\pi\sigma^*/S_0$ CI, then the CI would be avoided and dissociation would follow the adiabatic route to *p*-YPhS(\tilde{A}) + D fragments.⁵ This thereby provided a rationale for the finding that the relative yield of *p*-YPhS(\tilde{A}) products was greatest in cases where the S_0 minimum energy geometry (as predicted by the DFT calculations) was furthest from $\phi = 0^\circ$.

This article re-explores the dynamics of S–H bond fission following photoexcitation of PhSH and presents new experimental data for three *p*-substituted thiophenols (with Y

= F, CH₃, and MeO) obtained by H (Rydberg) atom photofragment translational spectroscopy (HRA-PTS) at many different excitation wavelengths between $305 \geq \lambda_{\text{phot}} \geq 240$ nm. This expands upon the prior data collected at 243.1 nm,⁵ which is reassessed in light of recent microwave studies that determine $\phi = 0^\circ$ in the S_0 state of *p*-FPhSH.¹⁵ An accurate determination of $\Delta E(\text{PhS}(\tilde{A}-\tilde{X}))$ from photodetachment studies of the thiophenolate anion¹⁶ allows reconsideration of the energy splitting value derived by Devine et al.,⁶ and of the nuclear motions that mediate branching at the $1^1\pi\sigma^*/S_0$ CI (which are implicit in determining this value from HRA-PTS data). The ab initio wavepacket calculations by Venkatesan et al.¹⁷ provide additional guidance in unraveling and refining the photofragmentation mechanisms of PhSH. Further, in light of the recent reappraisal of the photodissociation dynamics of phenol from $1^1\pi\pi^*$ excited levels in terms of H atom tunneling under the $1^1\pi\pi^*/1^1\pi\sigma^*$ CI,^{1,18,19} we investigate the extent to which an analogous tunneling mechanism contributes in the dissociation dynamics of *p*-YPhSH molecules. The present results show that the branching between H + *p*-YPhS \tilde{X} and \tilde{A} state products is dependent on both the excitation energy and the chemical substituent. The experiments are supported by new complete active space with second order perturbation theory (CASPT2) potential energy cuts (PECs) in the S–H dimension for the ground and excited states of PhSH. The energy barrier for rotation of the SH moiety about the C–S bond (E_{barrier}) in the S_0 state of each *p*-YPhSH molecule was investigated with high-level coupled cluster with single, double, and perturbative triple excitations using the F12 ansatz (CCSD(T)(F12*)) computations. The vertical excitation energies to, and corresponding barriers in, the $1^1\pi\pi^*$, $1^1\pi\sigma^*$, and $2^1\pi\pi^*$ excited states were evaluated with equation-of-motion coupled cluster with single and double excitations (EOM-CCSD) calculations in PhSH and the series of *p*-YPhSH molecules.

2. METHODS

2.1. Experimental Section. The HRA-PTS experimental setup has been described extensively before.^{9,20} *p*-CH₃PhSH (98%, Sigma Aldrich) and *p*-MeOPhSH (97%, Sigma Aldrich) are solids at room temperature and were heated to 70 and 50 $^\circ\text{C}$, respectively, to generate sufficient vapor pressure. Liquid *p*-FPhSH (98%, Sigma Aldrich) was placed into the finger of a bulb. The resulting vapor pressures were each seeded in ~ 700 Torr of Ar. These individual gas mixtures were pulsed through a solenoid valve into vacuum to create a molecular beam, which was subsequently skimmed and intersected by the frequency doubled output of a tunable nanosecond pulsed photolysis laser ($305 \geq \lambda_{\text{phot}} \geq 240$ nm).

H atom photoproducts formed in the interaction region were double-resonantly excited $\delta t \sim 10$ ns later, via the 2p state, by 121.6 nm (Lyman- α) radiation, and then to a high Rydberg state ($n \sim 80$) using a ~ 366 nm photon. Any accidental prompt ions formed within the interaction region were extracted using a biased deflector plate that straddles the interaction region. Rydberg-tagged H atoms that fly the known distance, d , to the detector are field ionized upon passing through a grounded mesh and detected. H atom time-of-flight (TOF) spectra are then converted into total kinetic energy release (TKER) spectra using eq 1:

$$\text{TKER} = \frac{1}{2} m_{\text{H}} \left(1 + \frac{m_{\text{H}}}{m_{\text{R}}} \right) \left(\frac{d}{t} \right)^2 \quad (1)$$

where m_{H} is the mass of the hydrogen atom (1.00794 u.), m_{R} is the mass of the assumed cofragment, ($p\text{-CH}_3\text{PhS} = 123.195$ amu, $p\text{-FPhS} = 127.159$ amu, and $p\text{-MeOPhS} = 139.194$ amu), and t is the time taken for the H atoms to travel from the interaction region to the detector. A t^{-3} Jacobian was applied when transforming the measured TOF signal intensities into TKER space.

TKER dependent product recoil anisotropy parameters, $\beta(\text{TKER})$, were obtained from analysis of spectra obtained with the polarization vector of the photolysis pulse, $\varepsilon_{\text{phot}}$ set at $\theta = 0$, 90 , and 54.7° to the TOF axis (achieved using an appropriately oriented double-Fresnel rhomb), as described in the Supporting Information.

H atom photofragment excitation (PHOFEX) spectra were recorded by scanning λ_{phot} in the presence of the Lyman- α laser pulse (and the 364.7 nm fundamental radiation from which it derives), while monitoring the H^+ ion yield using a small time-of-flight (TOF) mass spectrometer.

2.2. Computational and Theoretical Section. The S–H torsional coordinate of the ground state PES was explored with several ab initio methods for $p\text{-YPhSH}$ ($\text{Y} = \text{CH}_3$, F, and MeO) and bare PhSH. The dihedral angle, ϕ , was incremented and fixed at 15° intervals between $0 \leq \phi \leq 90^\circ$. The rest of the geometry was optimized using Møller–Plesset perturbation theory (MP2)^{21,22} with the aug-cc-pVTZ basis for the C, H, F, and O atoms,²³ and the aug-cc-p(T+d)Z basis set for the S atom.²⁴ The potentials in the ϕ coordinate are extremely shallow, so the convergence criteria were tightened to force the gradient on all atoms to be $<1 \times 10^{-6}$ a.u. Single-point energies were computed at these optimized geometries with the density fitted MP2-F12 (DF-MP2-F12)²⁵ and CCSD(T)(F12*)^{26,27} methods, again using the aug-cc-pVTZ and aug-cc-pV(T+d)Z basis set combination. For the resolution of the identity approximation intrinsic to the F12 methods, the aug-cc-pVTZ MP2 auxiliary basis was used as the complementary auxiliary basis set. The aug-cc-pVQZ auxiliary basis was used for density fitting for the MP2 integrals and the aug-cc-pVTZ basis for the integrals contributing to the Fock matrix. EOM-CCSD²⁸ vertical excitation energies for the first three singlet excited states (two in the case of $p\text{-MeOPhSH}$) were calculated over the full range of $0 \leq \phi \leq 90^\circ$ at the respective ground state optimized MP2 geometries. The excited state torsional barriers are calculated using the optimized S_0 geometries and thus represent upper limits. The transition dipole moments (TDMs) and oscillator strengths from S_0 were also calculated for these excited states, again using the EOM-CCSD methodology. Rotation about the C–C bond of the methyl group in $p\text{-CH}_3\text{PhSH}$ was neglected since a combined microwave and ab initio study found the barrier for such motion to be small,²⁹ we use this finding to justify treating the CH_3 group as a free-rotor.

DFT calculations were performed in Turbomole³⁰ to correct the torsional barriers on the S_0 and $1^1\pi\pi^*$ PESs for zero-point energy (ZPE) effects of the other $3N - 7$ vibrations. These corrected torsional potentials were used to generate solutions to the one-dimensional Schrödinger equation. The resulting levels were used to generate the ZPE-corrected barrier heights and Franck–Condon factors (FCFs). Full details of these calculations are given in the Supporting Information.

Complete active space self-consistent field (CASSCF)³¹ calculations were used to explore the electronic structure of

PhSH (in a planar configuration and the C_s point group) as a function of the S–H bond stretch ($R_{\text{S-H}}$) coordinate. A ten electrons in ten orbitals (10/10) active space was used, comprising the three ring π , the S–H σ , and the $\text{S}(3p_x)$ conjugated lone pair occupied orbitals, and the three ring π^* , the S–H antibonding σ^* , and the $\text{S}(4s)$ Rydberg virtual orbitals. This active space is similar to that used by Venkatesan et al.,¹⁷ but also explicitly includes the $4s$ Rydberg orbital. The same basis set as described for the ground state MP2 calculations was used, with additional s and p diffuse functions on the S atom, to allow for a better description of any valence–Rydberg (e.g., $1^1\pi\sigma^* - 1^1\pi 4s$) interactions. We henceforth refer to this basis as aug(S)-cc-pVTZ. This basis is superior to that used previously,¹⁷ as it includes a full set of diffuse aug-functions on C and H atoms. The S_0 , $1^1\pi\sigma^*$, $1^1\pi\pi^*$, and $2^1\pi\pi^*$ states were computed with CASSCF and each state-averaged with S_0 . The geometries of the ground and excited states were optimized for given values of $R_{\text{S-H}}$. To allow for some treatment of dynamical correlation effects, CASPT2^{32,33} single-point energies (with a 0.5 a.u. imaginary level shift) were then performed at these optimized geometries. MP2, DF-MP2, CASSCF, CASPT2, CCSD, EOM-CCSD, and CCSD(T)(F12*) calculations were performed in Molpro.³⁴

Ground state harmonic (and anharmonically corrected) wavenumbers for the normal mode vibrations of all the $p\text{-YPhS}(\tilde{X})$ radicals were calculated in Gaussian,³⁵ at the DFT/B3LYP level with a 6-311+G** basis set,³⁶ to aid assignment of the levels populated in the radical photoproducts. This methodology has proven successful in the assignment of product TKER spectra arising from X–H bond fission in many heteroaromatic molecules.^{2,7,12,13,19,20} The $p\text{-FPhS}$ radical has C_{2v} symmetry; by enforcing this constraint, it was thus also possible to calculate the harmonic wavenumbers of the $p\text{-FPhS}(\tilde{A})$ state, albeit at the minimum energy geometry of the \tilde{X} state radical.

3. RESULTS AND DISCUSSION

3.1. Computational Results. Figure 1 displays the CASPT2(10/10)/aug(S)-cc-pVTZ PECs as a function of $R_{\text{S-H}}$ for PhSH. These PECs are qualitatively similar to those published recently¹⁷ but differ quantitatively due to the different methodologies employed. The present study employs a slightly larger active space, incorporating explicitly the $4s$ Rydberg orbital, as well as the full aug-cc-pVTZ basis set on C and H atoms. The two sets of PECs are not directly comparable as the current calculation allows for geometry relaxation of the phenyl ring at each S–H bond distance for each excited state, whereas the earlier calculations fixed the ring geometry to that of the S_0 minimum energy structure.¹⁷ This leads to different excitation energies for the $1^1\pi\pi^*$ and $1^1\pi\sigma^*$ states; the present calculations predict an adiabatic energy separation in the vFC region of 0.24 eV between these states (cf., 0.45 eV in ref 17) and a lower minimum energy crossing point between these PESs, which is important to the ensuing excited state dynamics.

Examination of Figure 1 reveals that the PECs of PhSH along $R_{\text{S-H}}$ have many similarities with those calculated (at the same level of theory) for the O–H stretch in phenol.¹⁹ There are also several key differences, however. The vertical excitation energy of the $1^1\pi\sigma^*$ state in PhSH is significantly lower than in PhOH and close to the minimum of the $1^1\pi\pi^*$ state. This has the net effect of placing the $1^1\pi\pi^*/1^1\pi\sigma^*$ CI at an energy of ~ 4.4 eV (i.e., ~ 1.1 eV lower than in PhOH).^{19,37,38} Further, there is no noticeable shelf in the vFC region of the $1^1\pi\sigma^*$ PEC,^{2,39}

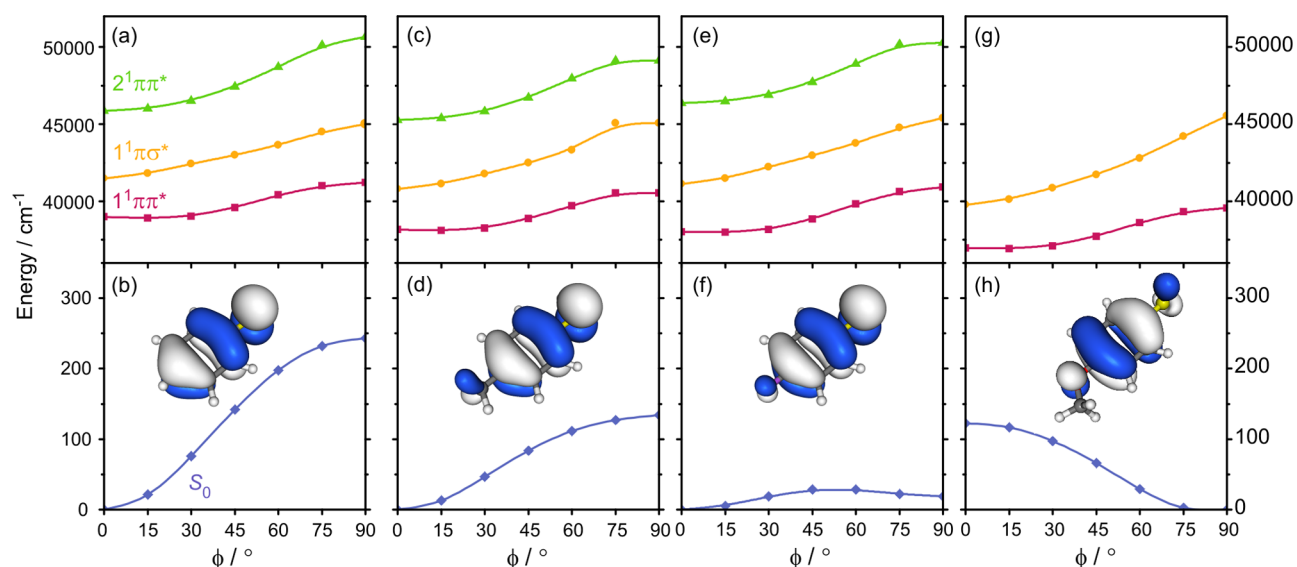


Figure 2. Torsional PECs for the S_0 , $1^1\pi\pi^*$, $1^1\pi\sigma^*$, and $2^1\pi\pi^*$ states of (a,b) PhSH, (c,d) p -CH₃PhSH, (e,f) p -FPhSH, and (g,h) p -MeOPhSH. The HOMO for each molecule is also displayed in the appropriate lower panel. The S_0 PECs were calculated at the CCSD(T)(F12*)/aug-cc-pVTZ level, whereas those for the excited states were calculated using the EOM-CCSD/aug-cc-pVTZ method.

Table 1. Calculated Ground State Minimum Energy Values of ϕ (in deg) and the Barrier Heights Associated with Rotation around the C–S Bond, E_{barrier} (in cm^{−1}), Together with Previous Calculated and Experimental Values

	PhSH		Y = CH ₃		Y = F		Y = MeO	
	E_{barrier}	ϕ_{min}	E_{barrier}	ϕ_{min}	E_{barrier}	ϕ_{min}	E_{barrier}	ϕ_{min}
MP2 ^a	270	0	198	0	71	0	35	75
DF-MP2-F12 ^a	235	0	238	0	45	0	9	0
CCSD ^a	152	0	43	0	74	90	220	90
CCSD(F12*) ^a	196	0	80	0	42	90	182	90
CCSD(T)(F12*) ^a	243	0	134	0	28	0	123	90
CCSD(T)(F12*) + ZPE ^a	265	0	145	0	40	0	106	90
DFT/B3LYP ^b	~275	0			~27	31	~175	73
DFT/B3P86 ^c	~415	0	~287	0			~65	70
CASPT2 ^d	348	0						
experiment ^{e,f}	267 ^{e,f}	0			63 ^f	0		

^aThis study: all calculations used the aug-cc-pVTZ basis set, see text for details. ^bReference 5: DFT/B3LYP/6-311++G(d,p). ^cReference 14: DFT/B3P86/6-311++G(3df,3pd). ^dReference 17: CASPT2/extended-cc-pVTZ calculation. ^eReference 41: fitted to microwave data. ^fReference 15: fitted to microwave data.

implying that the avoided crossing between the $1^1\pi_4$ s and $1^1\pi\sigma^*$ potentials is weaker in PhSH than for the analogous $1^1\pi_3$ s and $1^1\pi\sigma^*$ PESs in PhOH. Additionally, the $1^1\pi\sigma^*/S_0$ CI occurs at a longer bond length ($R_{\text{S-H}} \sim 2.8$ Å; cf., $R_{\text{O-H}} \sim 2.0$ Å in PhOH), reflecting the concomitant lowering of the $1^1\pi\sigma^*$ PEC, due to the weaker S–H bond strength (~ 2000 cm^{−1} smaller than $D_0(\text{PhO-H})$)^{6,12} and the smaller energy splitting between the \tilde{X} and \tilde{A} states of the PhS radical (~ 4000 cm^{−1} less than the equivalent splitting in PhO).^{6,13}

Figure 2 displays PECs along the torsional coordinate for the ground and lowest singlet excited states of PhSH (panels a and b) and p -YPhSH (Y = (c,d) CH₃, (e,f) F, and (g,h) MeO). The S_0 potentials, displayed in the lower panels, are calculated at the CCSD(T)(F12*)/aug-cc-pVTZ level, and the excited state surfaces (shown in the upper panels) are calculated at the EOM-CCSD/aug-cc-pVTZ level. The differences in the absolute excited state energies, cf., those shown in Figure 1, arise from the ring-relaxation in the CASPT2 excited state geometries (for PhSH), whereas the EOM-CCSD calculations were computed by varying ϕ , while holding the rest of the

structure at the S_0 optimized geometry. Calculations using the CCSD(T) method are generally considered the gold standard in terms of accuracy⁴⁰ but require the use of a very large (and therefore computationally prohibitive) number of basis functions for the size of molecule in this study. Here, the F12* ansatz is employed to circumvent this problem,²⁶ facilitating computations with an accuracy that extrapolates toward the basis set limit, but at significantly lower cost. The barrier height, E_{barrier} in the respective S_0 states and the dihedral angle, ϕ_{min} , associated with the minimum energy geometry are also listed in Table 1.

Concentrating first on the S_0 PESs, $\phi_{\text{min}} = 0^\circ$ for Y = H, CH₃, and F when calculated at the MP2, DF-MP2-F12*, and CCSD(T)(F12*) methods. The CCSD method returns $\phi_{\text{min}} = 90^\circ$ for p -FPhSH, highlighting that inclusion of (perturbative) triple excitations is essential in order to predict the electronic energies correctly. Similar variation in the predicted ϕ_{min} value with choice of computational method (and basis set) has been noted previously.¹⁷ The CCSD(T)(F12*)/aug-cc-pVTZ barrier heights and ϕ_{min} values for PhSH and p -FPhSH agree with

Table 2. Optimized excited state energies (in eV) for the $1^1\pi\pi^*$, $1^1\pi\sigma^*$ and $2^1\pi\pi^*$ states of PhSH calculated at the CASPT2/aug-cc-pVTZ level. EOM-CCSD/aug-cc-pVTZ vertical excitation energies (in eV), oscillator strengths, f , and E_{barrier} (in cm^{-1}) are given for PhSH and p -YPhSH ($Y = \text{CH}_3$, F and MeO)

state	CASPT2				EOM-CCSD								
	PhSH		PhSH		p -CH ₃ PhSH			p -FPhSH			p -MeOPhSH		
	energy	energy	f	E_{barrier}	energy	f	E_{barrier}	energy	f	E_{barrier}	energy	F	E_{barrier}
$1^1\pi\pi^*$	4.25	4.83	0.004	2213	4.73	0.007	2426	4.71	0.016	2892	4.90	0.012 ^a	2626
$1^1\pi\sigma^*$	4.49	5.14	0.003	3519	5.06	0.002	3931	5.10	0.002	4264	5.65	0.006 ^a	5767
$2^1\pi\pi^*$	4.97	5.69	0.233	4797	5.61	0.264	3720	5.75	0.210	3913			

^aThe oscillator strengths for p -MeOPhSH were computed using the aug-cc-pVDZ basis set in order to make the calculation computationally tractable. The vertical excitation energies were calculated using the aug-cc-pVTZ basis set.

fits to microwave data, and after the inclusion of ZPE effects, the agreement is excellent.^{15,41} Inclusion of ZPE effects leads to a slight increase of E_{barrier} for PhSH, p -CH₃PhSH, and p -FPhSH, but a decrease in the case of p -MeOPhSH (see Table 1, along with Supplementary Tables S1 and S2 for the ZPE-corrected barriers in the $1^1\pi\pi^*$ state and the calculated torsional levels, respectively). The E_{barrier} and ϕ_{min} values for $Y = \text{F}$ and MeO returned by the present calculations contradict the earlier DFT/B3LYP results⁵ but replicate the available microwave data (for $Y = \text{F}$ ¹⁵) well. For $Y = \text{MeO}$, the CCSD(T)(F12*)/aug-cc-pVTZ calculations predict $\phi_{\text{min}} = 90^\circ$. Unfortunately, there is no direct experimental data to validate this result, but given the success of our CCSD(T)-(F12*)+ZPE/aug-cc-pVTZ calculations in predicting ϕ_{min} and E_{barrier} for PhSH and p -FPhSH, where lower levels of theory performed poorly,^{5,14} we expect this method to be the most accurate predictor.

Henceforth, we focus largely on results obtained using the CCSD(T)(F12*)+ZPE/aug-cc-pVTZ method. The values of E_{barrier} decline across the series PhSH > p -CH₃PhSH > p -FPhSH, with p -FPhSH displaying shallow minima at both $\phi = 0$ and 90° , while the lowest energy configuration of p -MeOPhSH is predicted at $\phi = 90^\circ$. Our best reasoning for the nonplanar minimum energy geometry of p -MeOPhSH focuses on the stability of the highest occupied molecular orbital (HOMO). The HOMO of each molecule (see Figure 2) is formed mainly from the benzene $2p_x$ orbital, a contribution from the sulfur atom or the SH bond, and a varying contribution from the p -Y substituent. The Y substituent contributes most (in the form of a $2p_x$ lone pair) in the case that $Y = \text{MeO}$. As the electron donating ability of the p -Y substituent increases, $Y = \text{H} < \text{CH}_3 < \text{F} < \text{MeO}$, the relative stability of the $\phi = 0^\circ$ structure over the $\phi = 90^\circ$ structure decreases, such that for MeO, the $\phi = 90^\circ$ structure is lower in energy. In the case that $Y = \text{H}$, CH_3 , or F , the sulfur based contribution to the HOMO in the minimum energy configuration is the $3p_x$ S lone pair, whereas when $Y = \text{MeO}$, it is replaced by the S–H σ^* orbital. Thus, in the planar configuration of p -MeOPhSH, the sulfur $3p_x$ and oxygen $2p_x$ lone pairs are both conjugated with the ring plane (see Supplementary Figure S1), and our barrier calculations show this is clearly destabilizing, presumably because too much π electron density is localized on the phenyl moiety. This is intuitive in terms of orbital overlap; the $2p_x(\text{O})$ – $2p_x$ orbital overlap is more effective than for $3p_x(\text{S})$ – $2p_x$. Ergo, if the S–H bond rotates out of the ring plane, some σ^* character is introduced into the HOMO (which is able to accept any excess electron density from the ring) and the conjugation with the $3p_x$ sulfur lone pair is relieved. Such nonplanar arrangements of the S–H bond relative to an aromatic ring plane are not limited

to thiophenols; similar behavior was revealed in our previous study of 2-methyl-3-thiofuran.⁴²

E_{barrier} is far greater in the excited states of all four molecules ($>2000 \text{ cm}^{-1}$, as shown in Table 2 and in the upper panels of Figure 2), and the minimum energy geometries lie at (or close to) $\phi = 0^\circ$. It is important to recognize that these E_{barrier} values likely represent upper bounds since the calculations are computed at the optimized S_0 geometries. The shapes and heights of the barriers calculated for the $1^1\pi\pi^*$ and $1^1\pi\sigma^*$ states of PhSH are in good agreement (E_{barrier} is $\sim 10\%$ smaller) with those derived in recent CASPT2/extended-cc-pVTZ calculations that enforced a rigid ring geometry.¹⁷ ZPE-corrected effective potentials along the torsional coordinate of the S_0 (eq S3, Supporting Information) and $1^1\pi\pi^*$ PESs were calculated for each molecule, allowing estimation of the FC activity in the torsional mode, τ_{SH} . The calculated τ_m^n FCFs were then weighted by the relative population in the torsional level with energy E_m (assuming a Boltzmann distribution over S_0 torsional states, and a temperature of 50 K) in order to illustrate the likely substructure contributing to the respective parent absorption spectra. This analysis shows that the extent of torsional activity upon photoexcitation is very sensitive to the relative values of ϕ_{min} in the S_0 and $1^1\pi\pi^*$ states, and to the magnitude of E_{barrier} in the S_0 state (see Figure S2 and accompanying text in the Supporting Information). The latter determines the amplitude of torsional motion in the S_0 molecule prior to photoexcitation (for a given Boltzmann weighting), while the former determines the dominant FC factors. For molecules like PhSH and p -CH₃PhSH (where $\phi_{\text{min}} \sim 0^\circ$ in both states) diagonal torsional transitions (i.e., transitions with $m = n$) are predicted to dominate (e.g., Supplementary Figure S2c,d), whereas, in the cases of p -FPhSH and, particularly, p -MeOPhSH (Supplementary Figure S2e,f), our FC analysis predicts a broad spread of torsional activity in the $1^1\pi\pi^* \leftarrow S_0$ absorption process.

Table 2 shows that the $1^1\pi\pi^* \leftarrow S_0$ transitions in PhSH and the three p -YPhSH molecules of interest have similar oscillator strengths. The TDM in each case lies in the ring plane and perpendicular to the C–S bond (i.e., along y) axis (see Figure 1). The $1^1\pi\sigma^* \leftarrow S_0$ transitions are weaker (but stronger than in phenol¹⁷). The orientation of the TDM vector in this case is sensitive to the orientation of the S–H bond relative to the ring plane (i.e., the angle ϕ); in PhSH p -CH₃PhSH and p -FPhSH, the $1^1\pi\sigma^* \leftarrow S_0$ TDM lies perpendicular to the plane of the molecule (i.e., along x), whereas in p -MeOPhSH, it is predicted to lie parallel to the C–S bond, along the z axis. In all cases, however, we note that the $1^1\pi\sigma^* \leftarrow S_0$ TDM vector is perpendicular to the S–H bond in the ground state minimum energy geometry.

3.2. UV Absorption Spectroscopy. Room temperature UV absorption spectra of the three *p*-YPhSH molecules, measured in the range $310 \geq \lambda \geq 200$ nm, are shown in Figure 3: Y = (a) CH₃, (b) F, and (c) MeO. All display similar features

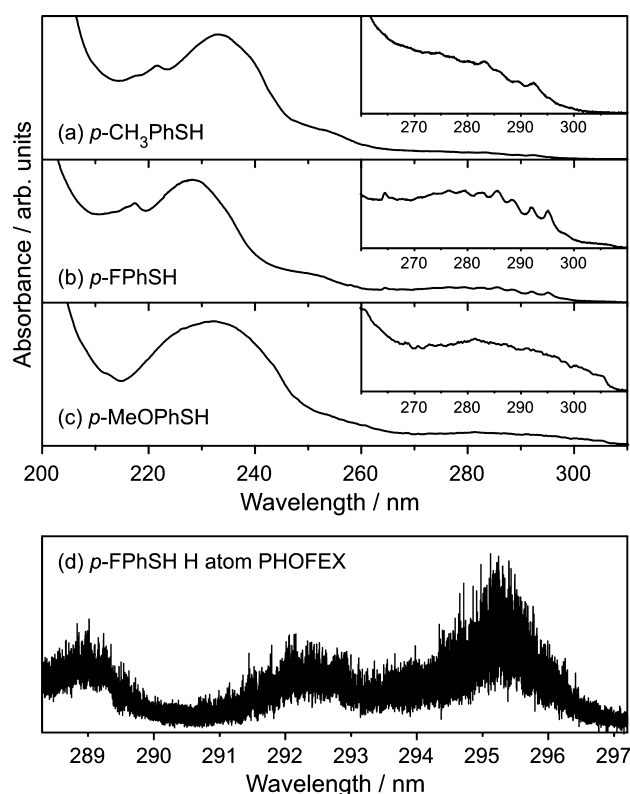


Figure 3. Room temperature UV absorption spectra of (a) *p*-CH₃PhSH, (b) *p*-FPhSH, and (c) *p*-MeOPhSH in the range 310–200 nm. The 310–260 nm regions are shown on an expanded vertical scale in the respective insets. (d) Long wavelength end of the H atom PHOFEX spectrum following UV excitation of jet-cooled *p*-FPhSH molecules.

and broadly mirror the spectrum of PhSH.^{6,43} The absorption onset shifts to longer wavelengths in the order CH₃ < F < MeO, consistent with the predicted EOM-CCSD/aug-cc-pVTZ $1^1\pi\pi^* \rightarrow S_0$ vertical excitation energies (see Figure 2 and Table 2). Each spectrum exhibits four recognizable features: a weak absorption at long wavelength (~ 305 – 265 nm) that shows some diffuse structure (most evident for Y = CH₃ and F (Figure 3a,b) on top of a continuous background signal, a smoothly increasing absorption as λ decreases between ~ 260 – 245 nm, a more intense feature centered ~ 230 nm, and an intense feature that rises at $\lambda < 210$ nm and maximizes outside the range of the recorded spectra.

3.3. Ion Time-of-Flight and H Atom Photofragment Excitation Spectroscopy. TOF spectra of ions formed from the photolysis laser interacting with the pulsed molecular beam alone, or in combination with the Lyman- α (and 364.7 nm) radiation, were recorded for each molecule at various wavelengths in the range $300 \geq \lambda_{\text{phot}} \geq 270$ nm. Negligible parent ion signal (i.e., m/z 124, 128, and 140 for Y = CH₃, F, and MeO, respectively) was observed in any case, in contrast to behavior seen previously with, for example, indole,⁴⁴ aniline,⁴⁵ or phenol.⁴⁶ Ion TOF spectra recorded in the presence of the Lyman- α radiation were all dominated by a peak at m/z 1. H atom PHOFEX spectra were acquired by measuring the m/z 1

peak intensity while scanning λ_{phot} from a wavelength slightly longer than the respective absorption onset. By way of illustration, Figure 3d shows the H atom PHOFEX spectrum arising from *p*-FPhSH. The maxima and minima of the evident undulations match well with those in the corresponding UV absorption spectrum (Figure 3b), and the latter therefore guided the choice of excitation wavelength for subsequent HRA-PTS studies, as in our previous PhSH study.⁶ While torsional fine structure may contribute to the spectral broadening (see section 3.1), the dominant factor is likely to be lifetime broadening.

3.4. H (Rydberg) Atom Photofragment Translational Spectroscopy. 3.4.1. *p*-CH₃PhSH.

Figure 4 displays repre-

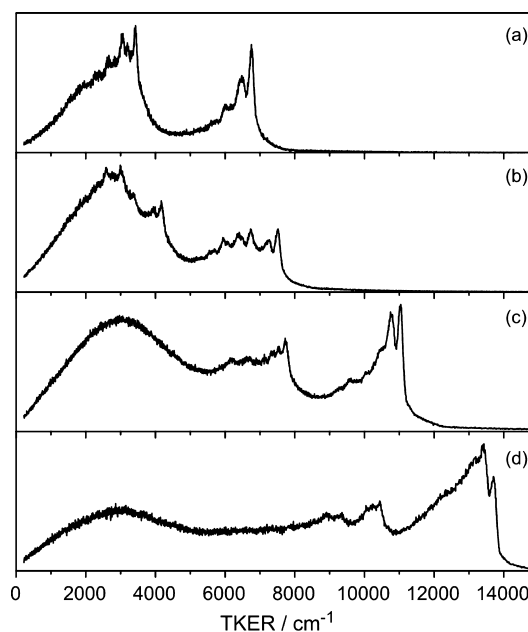


Figure 4. TKER spectra of the H + *p*-CH₃PhS products from photolysis of *p*-CH₃PhSH at λ_{phot} = (a) 292.5, (b) 286.2, (c) 260.0, and (d) 243.0 nm.

sentative TKER spectra for four different photolysis wavelengths. Figure 4a,b shows TKER spectra acquired at λ_{phot} = 292.5 and 286.2 nm and are representative of data recorded between $295 \geq \lambda_{\text{phot}} \geq 271$ nm. All such spectra were found to be most intense when ϵ_{phot} was aligned at $\theta = 0^\circ$, i.e., $\beta > 0$; the H atoms produced at these wavelengths recoil preferentially parallel to ϵ_{phot} and thus to the parent TDM.

Figure 4c,d displays data taken at λ_{phot} = 260.0 and 243.0 nm and are representative of TKER spectra acquired in the range $271 \text{ nm} \geq \lambda_{\text{phot}} \geq 243$ nm. The two structured components show preferential perpendicular recoil at these wavelengths, so ϵ_{phot} was aligned at $\theta = 90^\circ$ when recording the displayed spectra. A third, isotropic component peaking at $\text{TKER} \approx 3000 \text{ cm}^{-1}$ is also evident in Figure 4c,d. Such signal is characteristic of H atoms arising from a statistical dissociation process and plausibly arises from decay of molecules in highly vibrationally excited levels of the S_0 state populated after internal conversion and/or following multiphoton absorption into superexcited states.^{13,47} If we associate the fastest peak (i.e., the peak at TKER_{max}) in spectra recorded at numerous wavelengths between $295 \geq \lambda_{\text{phot}} \geq 235$ nm with formation of H + *p*-CH₃PhS(\tilde{X})_{*v*=0} products then, using eq 2

$$E_{\text{int}}(p\text{-CH}_3\text{PhSH}) + E_{\text{phot}} \\ = D_0(p\text{-CH}_3\text{PhS-H}) + \text{TKER}_{\text{max}} + E_{\text{int}}(p\text{-CH}_3\text{PhS}) \quad (2)$$

and defining the internal energy of the parent molecule, $E_{\text{int}}(p\text{-CH}_3\text{PhSH}) = 0$, we obtain an S–H bond strength, $D_0(p\text{-CH}_3\text{PhS}(\tilde{X})\text{-H}) = 27\,430 \pm 50 \text{ cm}^{-1}$. The energy separation between the two clusters of peaks is similar to $\Delta E(\text{PhS}(\tilde{A}-\tilde{X}))$,¹⁶ and the value $\Delta E(p\text{-CH}_3\text{PhS}(\tilde{A}-\tilde{X})) = 2992 \text{ cm}^{-1}$ returned by previous CASPT2(8/9)/aug-cc-pVTZ calculations.⁹ Thus, the sets of peaks at lower TKER are attributed to $\text{H} + p\text{-CH}_3\text{PhS}(\tilde{A})$ products. A similar analysis of this slower component in all measured TKER spectra, wherein we associate the fastest peak to formation of $\text{H} + p\text{-CH}_3\text{PhS}(\tilde{A})_{v=0}$ products (see later discussion), yields $D_0(p\text{-CH}_3\text{PhS}(\tilde{A})\text{-H})_{v=0} = 30\,750 \pm 50 \text{ cm}^{-1}$, and thus an energy separation between the ground and first excited states of the $p\text{-CH}_3\text{PhS}$ radical, $\Delta E(p\text{-CH}_3\text{PhS}(\tilde{A}-\tilde{X})) = 3320 \pm 50 \text{ cm}^{-1}$. It is normally trivial to replot TKER spectra in terms of the product internal energy, E_{int} . In the photodissociation of $p\text{-CH}_3\text{PhSH}$ (and the other $p\text{-YPhSH}$ molecules), however, we have two different active asymptotes yielding H atom products, and it proves more convenient to allocate separate E_{int} scales for the \tilde{X} and \tilde{A} state $p\text{-CH}_3\text{PhS}$ fragments.

Figure 5 shows E_{int} spectra from photolysis of jet-cooled $p\text{-CH}_3\text{PhSH}$ molecules in the range $295 \text{ nm} \geq \lambda_{\text{phot}} \geq 282.7 \text{ nm}$, arranged in descending order of photolysis wavelength. The product peak assignments are guided by the calculated (B3LYP/6-311+G**, with anharmonic correction) normal mode wavenumbers of the \tilde{X} state radical (see Supplementary Table S3), which are labeled using Wilson notation.⁴⁸ This labeling scheme has the advantage that it identifies modes according to specific nuclear displacements, rather than listing them in descending wavenumber and is particularly convenient here as it allows direct comparison of $p\text{-YPhS}$ radical (and $p\text{-YPhSH}$ parent) modes.

Figure 5a displays the E_{int} spectrum obtained at $\lambda_{\text{phot}} = 293.5 \text{ nm}$ (a wavelength longer than the peak of the first feature in the parent absorption spectrum (Figure 3a)) and shows that most of the $p\text{-CH}_3\text{PhS}(\tilde{X})$ products are formed in $v = 0$, with some modest population in $\nu_{18b} = 1$. ν_{18b} is predominantly an in-plane C–S bond wagging vibration (see Figure 6). Activity in this product mode is rationalized using the present CASSCF/CASPT2 calculations (for PhSH), which predict an internal C–S–H bond angle of $\sim 98^\circ$ in both the $1^1\pi\pi^*$ and $1^1\pi\sigma^*$ states. In the limit of axial recoil, any impulsive recoil from the departing H atom is imparted onto the S atom and essentially perpendicular to the C–S bond and is thus ideal for exciting ν_{18b} . A similar E_{int} spectrum is obtained upon tuning to $\lambda_{\text{phot}} = 292.5 \text{ nm}$ (resonant with the first peak in the parent absorption band), as shown in Figure 5b. The peak assigned to $\nu_{18b} = 1$ appears broader in this spectrum, and a third peak at higher E_{int} is more clearly evident. The increased breadth of the former and the appearance of the latter are attributed to population of levels carrying, respectively, one and two quanta of ν_{6a} , the lowest energy a_1 ring-breathing mode (see Figure 6 and Supplementary Table S3). The comparatively narrow width of these features indicates that the radical fragments are formed with only modest rotational excitation, which is as expected given the lightness of the departing H atom partner.

Assignments of the $p\text{-CH}_3\text{PhS}(\tilde{A})$ product vibrations were made by seeking self-consistency across the whole range of

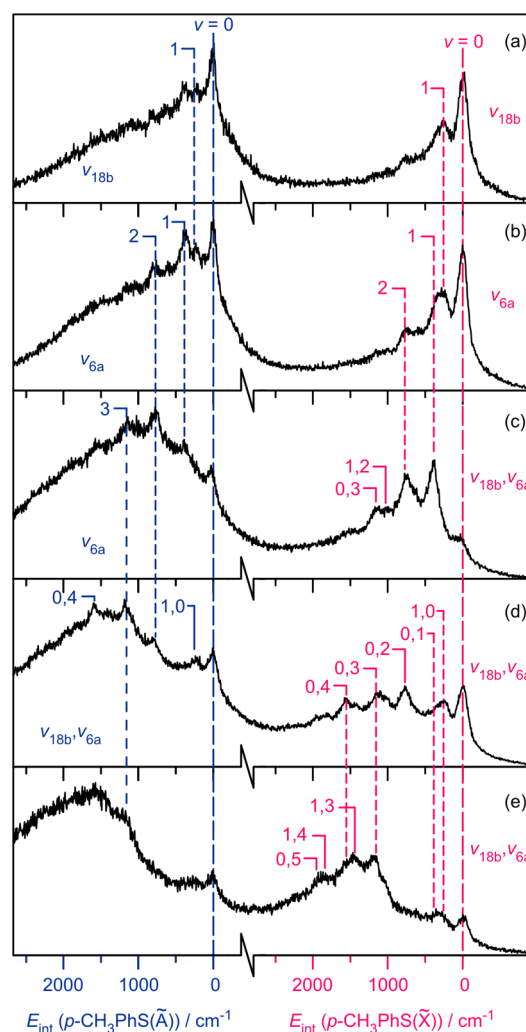


Figure 5. E_{int} spectra for \tilde{X} and \tilde{A} state $p\text{-CH}_3\text{PhS}$ radicals from photolysis of $p\text{-CH}_3\text{PhSH}$ molecules at $\lambda_{\text{phot}} =$ (a) 293.5, (b) 292.5, (c) 289.4, (d) 286.2, and (e) 282.7 nm. Color-coded vibrational mode assignments for both sets of radical products are festooned over each spectrum.

excitation wavelengths studied and were guided by the calculated $p\text{-CH}_3\text{PhS}(\tilde{X})$ normal mode wavenumbers (Supplementary Table S3). This latter assumption is justified by recognizing that the main difference in the electronic structures of the \tilde{X} and \tilde{A} states of the radical is simply the relative orientation of the SOMO (which is relatively disconnected from the ring π system). Self-consistency is achieved by assigning the fastest peak in the cluster attributed to $p\text{-CH}_3\text{PhS}(\tilde{A})$ products to population of the $v = 0$ level.

Such an assignment runs counter to that offered in the earlier HRA-PTS study of PhSH,^{6,7} wherein the equivalent peak was assigned to population of $\text{PhS}(\tilde{A})$ radicals with $\nu_{11} = 1$ (relative to an unobserved $v = 0$ origin). ν_{11} is the lowest energy b_1 (a'') nuclear motion of the PhS radical, and the rationale for the earlier assignment was based on symmetry arguments and normal mode calculations. The former we address first. The CI between the $1^1\pi\sigma^*$ and S_0 PESs at $R_{\text{S-H}} \sim 2.8 \text{ \AA}$ determines the branching between ground (diabatic) and excited (adiabatic) thiophenoxyl radical products.^{3,6,7,17} The electronic symmetries of the $1^1\pi\sigma^*$ and S_0 states are $1^1A''$ and $1^1A'$ (in the C_s point group), which correlate diabatically with, respectively, the $\text{H} + \text{PhS}(\tilde{X}^2B_1)$ and $\text{H} + \text{PhS}(\tilde{A}^2B_2)$ product asymptotes. In order

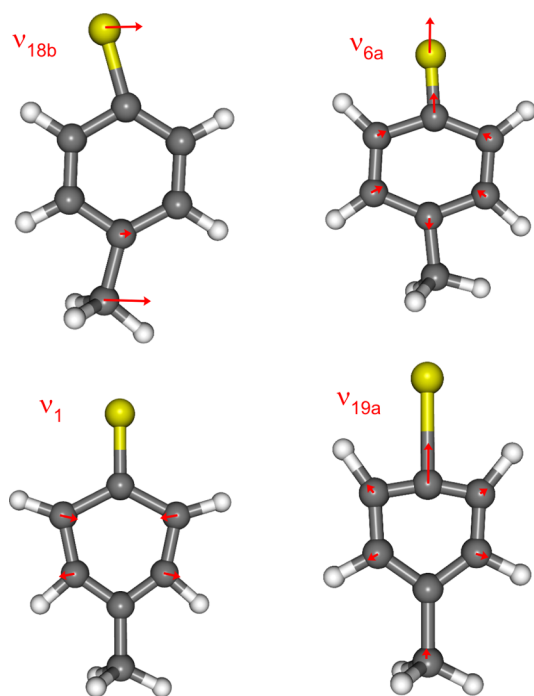


Figure 6. Nuclear motions associated with selected normal modes of the p -CH₃PhS radical populated in the present photolysis studies. Use of the Wilson labeling scheme⁴⁸ ensures that these illustrations are similarly applicable to the other p -YPhS radicals.

for flux to switch from the $1^1\pi\sigma^*$ ($1^1A''$) PES to the diabatic S_0 ($1^1A'$) PES, we require a nuclear coupling mode of a'' symmetry. This could be the S–H torsion (τ_{SH}), as predicted by Venkatesan et al., who show this mode to have the largest associated nonadiabatic coupling matrix element at the $1^1\pi\sigma^*/S_0$ CI.¹⁷ PhS(\tilde{A}) _{$\nu=0$} product formation would be expected if τ_{SH} is the nuclear motion that drives the coupling at the $1^1\pi\sigma^*/S_0$ CI since torsion is one of the three modes that disappear upon S–H bond fission. The earlier study⁶ employed PhS radical modes not calculated at the quoted level of theory. The two fastest peaks associated with PhS(\tilde{A}) products were assigned to population of the $\nu_{11} = 1$ and $\nu_{16a} = 1$ levels, both of which are primarily a'' ring twisting motions. If these skeletal modes were to mediate coupling at the $1^1\pi\sigma^*/S_0$ CI, one would expect to see these motions preserved upon S–H bond fission and mapping into the PhS(\tilde{A}^2B_2) product radicals (see Supplementary Figure S3).⁶ The present calculations of radical mode wavenumbers (at the appropriate level of theory) show that the spacing between the first two peaks in the cluster associated with PhS(\tilde{A}) products is in good accord with one quantum of ν_{18b} (the wavenumber of which was previously estimated to be ~ 60 cm^{−1} larger). The TKER_{max} peak can thus be consistently assigned to $\nu = 0$ products (see Supplementary Figure S3) and $\Delta E(\text{PhS}(\tilde{A}-\tilde{X}))$ redefined as 2960 ± 100 cm^{−1}, bringing the energy splitting derived by HRA-PTS⁶ and photodetachment¹⁶ experiments into very good accord and in-line with the predictions from recent theoretical studies.¹⁷ Given the observed dynamical similarities, we expect this rationale to apply to the whole series of p -YPhSH molecules.

Returning to p -CH₃PhSH, the peak assignments in Figure 5a,b imply formation of the *same* subset of vibrational levels in the \tilde{X} and \tilde{A} state radical products, reinforcing the view that the skeletal motions are established early in the dissociation process and prior to the $1^1\pi\sigma^*/S_0$ CI that controls the electronic

branching between the two product asymptotes.^{3,6,7,17} Figure 5c ($\lambda_{\text{phot}} = 289.4$ nm, resonant with the second peak in the UV absorption spectrum) displays a similar radical population distribution to that observed at $\lambda_{\text{phot}} = 292.5$ nm, but shifted to higher internal energy by one quantum of ν_{6a} . Here, it proves useful to consider the internal energy (E_{ex}) of the photoexcited parent molecule. Such analysis offers some insight into whether vibrational excitation evident in the final p -CH₃PhS products is likely to have originated from a mode promoted in the initial photoexcitation step. At $\lambda_{\text{phot}} = 289.4$ nm, E_{ex} is ~ 365 cm^{−1} relative to $\lambda_{\text{phot}} = 292.5$ nm (a wavelength resonant with the first peak in the parent absorption spectrum, which we associate with the $1^1\pi\pi^*-S_0$ origin). The corresponding wavenumber for ν_{6a} in the \tilde{X} state of the radical is 386 cm^{−1}. Thus, we propose that excitation at $\lambda_{\text{phot}} = 289.4$ nm populates a short-lived excited state resonance involving $\nu_{6a} = 1$ and that this motion carries through into the p -CH₃PhS products. Similar behavior is implicit in the results shown for $\lambda_{\text{phot}} = 286.2$ and $\lambda_{\text{phot}} = 282.7$ nm (see Figure 5d,e), and assignments are made by equivalent analyses.

The photodissociation dynamics observed in this long wavelength region can be understood in terms of initial population of an excited state capable of supporting (quasi-) bound vibrational levels. EOM-CCSD/aug-cc-pVTZ (see section 3.1) and CASPT2 calculations for PhSH (see Figure 1 and ref 17) and p -CH₃PhSH¹¹ all show that the $1^1\pi\pi^*$ state is the first excited singlet state in the vFC region. Thus, we conclude that long wavelength excitation results in population of Franck–Condon active levels of the $1^1\pi\pi^*$ state, which couple to the $1^1\pi\sigma^*$ PES and subsequently dissociate (see later discussion of nonadiabatic coupling at the $1^1\pi\pi^*/1^1\pi\sigma^*$ CI). Electronic branching into the radical products occurs at the $1^1\pi\sigma^*/S_0$ CI, but the skeletal nuclear motions orthogonal to the dissociation coordinate are determined in the $1^1\pi\pi^* \leftarrow S_0$ photoexcitation step and evolve adiabatically into the radical products. This understanding allows us to offer assignments for hitherto undefined features evident in the $1^1\pi\pi^*-S_0$ absorption spectrum of p -CH₃PhSH, as listed in Supplementary Table S6.

The E_{int} spectrum acquired at $\lambda_{\text{phot}} = 271.0$ nm (Figure 7a) shows an apparent reversal of the previous trend, where reducing the photolysis wavelength resulted in progressively more vibrationally excited radical products (e.g., Figure 5a–e). The most clearly resolved peaks in Figure 7a are assigned to population of the $\nu = 0$, $\nu_{6a} = 1$, $\nu_{18b} = 1$, and $\nu_{6a} = 1 + \nu_{18b} = 1$ levels of the \tilde{X} and \tilde{A} states of the p -CH₃PhS radical. Figure 7 shows three further E_{int} spectra, derived from H atom TOF spectra recorded at wavelengths between 260.0 and 243.0 nm. At $\lambda_{\text{phot}} = 260.0$ nm (Figure 7b), we observe formation of CH₃PhS(\tilde{X}) radicals in their $\nu = 0$, $\nu_{18b} = 1$, $\nu_{6a} = 1$, $\nu_{6a} = 1 + \nu_{18b} = 1$, $\nu_1 = 1 + \nu_{6a} = 1$, and $\nu_1 = 1$ levels. \tilde{A} state products are identified in the same vibrational levels. ν_1 is another a_1 symmetric ring breathing motion (see Figure 6). Data acquired at progressively shorter wavelengths, $\lambda_{\text{phot}} = 250.0$ and 243.0 nm (Figures 7c,d), all show a similar product distribution to that at $\lambda_{\text{phot}} = 260.0$ nm (Figure 7b), but with a small increase in vibrational excitation. The energy introduced into the molecule increases by ~ 3000 cm^{−1} upon reducing λ_{phot} from 271 and 243 nm, yet inspection of the corresponding E_{int} spectra suggests that the average vibrational energy in the radical products increases by only ~ 500 cm^{−1}. This implies that most of the additional photon energy is partitioned into product translation, consistent with direct excitation to, and dissociation on, a repulsive PES. CASPT2 calculations¹¹ predict

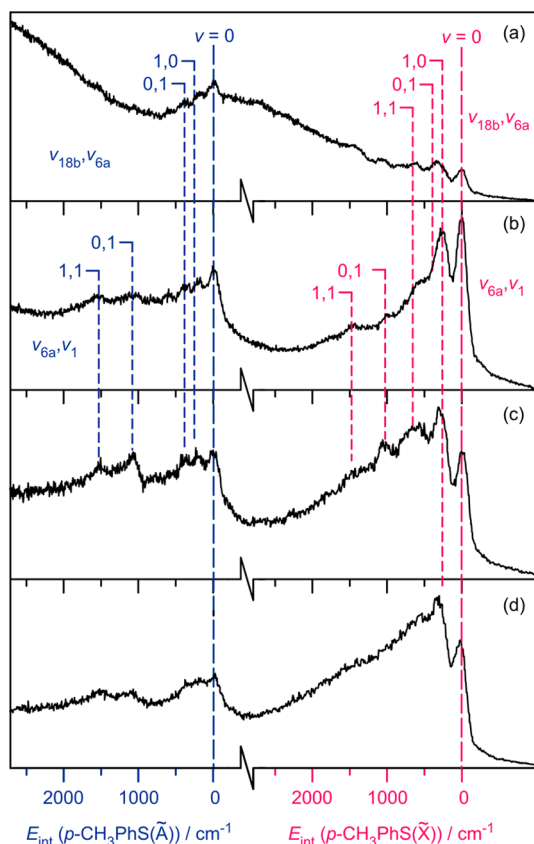


Figure 7. E_{int} spectra of the $p\text{-CH}_3\text{PhS}(\tilde{\text{X}})$ and $p\text{-CH}_3\text{PhS}(\tilde{\text{A}})$ products from photolysis of jet-cooled $p\text{-CH}_3\text{PhSH}$ molecules at $\lambda_{\text{phot}} =$ (a) 271.0, (b) 260.0, (c) 250.0, and (d) 243.0 nm. Color-coded vibrational mode assignments for both sets of radical products are shown above each spectrum.

the onset for $1^1\pi\sigma^* \leftarrow S_0$ absorption in $p\text{-CH}_3\text{PhSH}$ at ~ 270 nm, and the $1^1\pi\sigma^*$ PES is repulsive with respect to S–H bond extension (recall Figure 1). We therefore deduce that the dissociation dynamics implicit in the E_{int} spectra shown in Figure 7 are the result of direct excitation to this state.

3.4.2. $p\text{-FPhSH}$. Jet-cooled $p\text{-FPhSH}$ molecules were also excited at many UV wavelengths in the range $295.2 \geq \lambda_{\text{phot}} \geq 243.1$ nm. The resulting TKER spectra display very similar trends to those shown by $p\text{-CH}_3\text{PhSH}$, and thus only representative samples of these data are shown in the main article (the remainder appear as Figures S5 and S6 in the Supporting Information). The TKER spectra show a vibrational structure attributable to both $\tilde{\text{X}}$ and $\tilde{\text{A}}$ state $p\text{-FPhS}$ radicals. From these data, we derive $D_0(p\text{-FPhS-H}) = 27\,420 \pm 50$ cm^{-1} and $\Delta E(p\text{-FPhS}(\tilde{\text{A}}-\tilde{\text{X}})) = 3420 \pm 50$ cm^{-1} by assigning the TKER_{max} peak within each of the respective clusters to $v = 0$ products (as per the discussion in section 3.4.5.1). Figure 8 shows illustrative E_{int} spectra obtained at (a) the $1^1\pi\pi^*-S_0$ origin ($\lambda_{\text{phot}} = 295.2$ nm), (b) a vibrationally excited level of the $1^1\pi\pi^*$ state ($\lambda_{\text{phot}} = 284.9$ nm), and (c) when the $1^1\pi\sigma^*$ state is populated directly ($\lambda_{\text{phot}} = 258.0$ nm). The population distributions in the $\tilde{\text{X}}$ and $\tilde{\text{A}}$ state $p\text{-FPhS}$ radicals formed at the longest excitation wavelength are reminiscent of those found in the $p\text{-CH}_3\text{PhS}$ radicals formed when exciting the respective origin (Figure 5a,b), exhibiting selective, but modest, vibrational excitation in modes ν_{18b} and ν_{6a} . The E_{int} spectrum shown in Figure 8b reveals selective population of the $\nu_{13} = 1$ level of both the $\tilde{\text{X}}$ and $\tilde{\text{A}}$ state radical products (ν_{13} is another

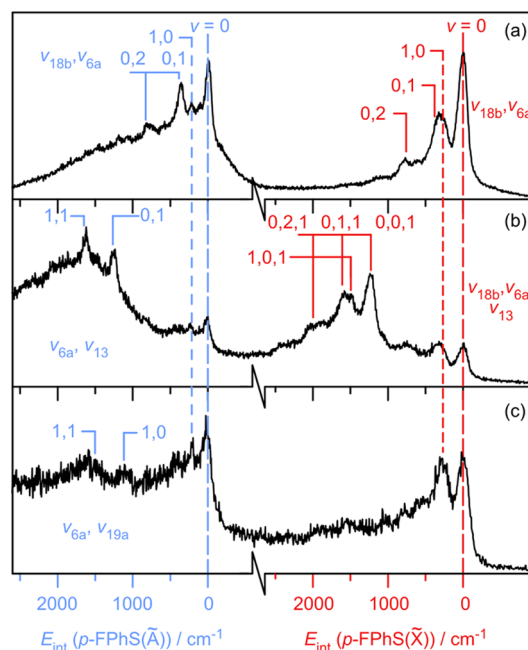


Figure 8. E_{int} spectra for $p\text{-FPhS}(\tilde{\text{X}})$ and $p\text{-FPhS}(\tilde{\text{A}})$ products from photolysis of jet-cooled $p\text{-FPhSH}$ molecules at $\lambda_{\text{phot}} =$ (a) 295.2, (b) 284.9, and (c) 258.0 nm. Color-coded vibrational mode assignments for both sets of radical products are shown above each spectrum.

symmetric ring breathing mode). As for $p\text{-CH}_3\text{PhSH}$, we conclude that 284.9 nm excitation of $p\text{-FPhSH}$ populates the $1^1\pi\pi^*_{\nu_{13}=1}$ level and that this nuclear motion is retained en route from the excited parent molecule to radical products. Tuning to shorter λ_{phot} (i.e., to higher internal energies in the $1^1\pi\pi^*$ state) yields radical products with progressively greater internal excitation (see Supplementary Figure S5 and Table S6), providing further illustration of the adiabatic mapping of parent skeletal motion into the radical products. Figure 8c is typical of TKER spectra acquired at energies above the threshold for direct population of the $1^1\pi\sigma^*$ state. The product vibrational population distributions are similar to those observed when exciting the corresponding state in $p\text{-CH}_3\text{PhSH}$ with the additional population of ν_{19a} levels (see Figure 6) and, as in that case, we find that most of the additional photon energy is partitioned into product translation (see Supplementary Figure S6). One obvious difference between the dynamics displayed by $p\text{-FPhSH}$ and $p\text{-CH}_3\text{PhSH}$ is the $\tilde{\text{X}}/\tilde{\text{A}}$ branching ratio following direct excitation to the $1^1\pi\sigma^*$ state: $p\text{-FPhSH}$ has a far greater tendency to follow the adiabatic fragmentation pathway to $\tilde{\text{A}}$ state products.

3.4.3. $p\text{-MeOPhSH}$. The UV absorption (Figure 3c) and H atom PHOFEX spectra of $p\text{-MeOPhSH}$ display no obvious structure at long wavelengths, unlike those for $p\text{-FPhSH}$ and $p\text{-CH}_3\text{PhSH}$. H atom TOF (and thus TKER) spectra were therefore recorded at ~ 5 nm intervals starting from the long wavelength absorption onset. Figure 9 displays E_{int} spectra acquired between $305.0 \geq \lambda_{\text{phot}} \geq 255.0$ nm. The E_{int} scale was established using the same analysis and assignment routines as for the other $p\text{-YPhSH}$ molecules. The TKER_{max} feature in both of the two clusters of peaks in each TKER spectrum was attributed to $\text{H} + p\text{-MeOPhS}(\tilde{\text{X}} \text{ and } \tilde{\text{A}})_{v=0}$ products. Such analysis yielded $D_0(p\text{-MeOPhS-H}) = 26\,860 \pm 50$ cm^{-1} and the energy splitting $\Delta E(p\text{-MeOPhS}(\tilde{\text{A}}-\tilde{\text{X}})) = 4000 \pm 50$ cm^{-1} . The E_{int} spectrum at $\lambda_{\text{phot}} = 305.0$ nm shows peaks attributable

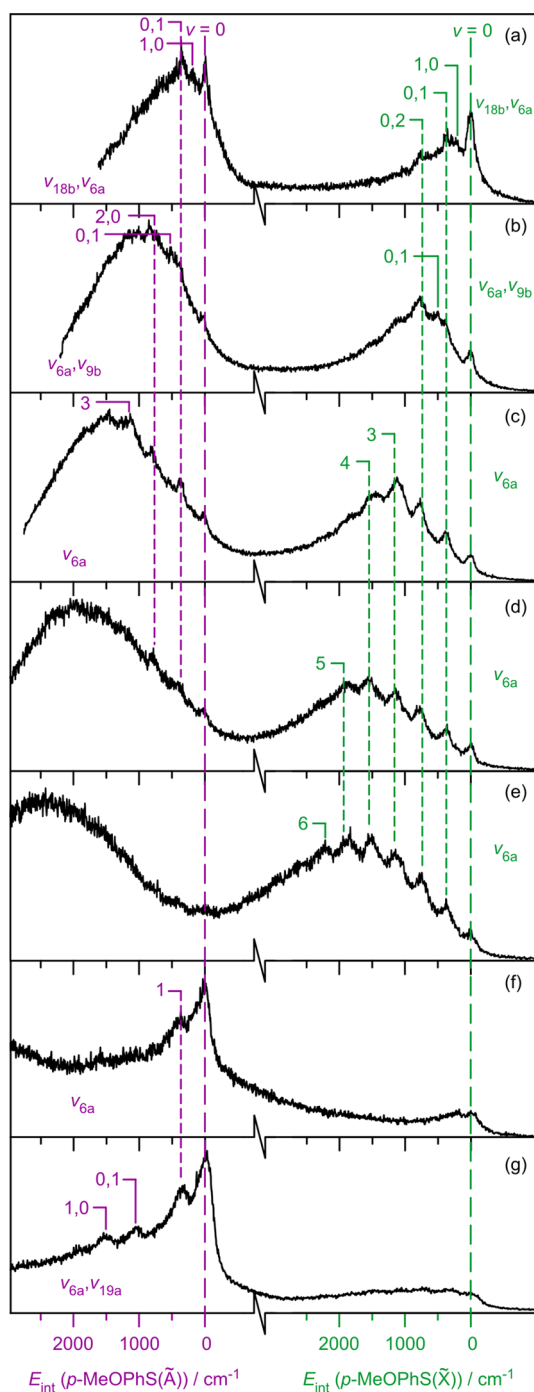


Figure 9. E_{int} spectra for \tilde{X} and \tilde{A} state p -MeOPhS radical products from photolysis of jet-cooled p -MeOPhSH molecules at λ_{phot} = (a) 305.0, (b) 300.0, (c) 297.5, (d) 290.0, (e) 280.0, (f) 265.0, and (g) 255.0 nm. Color-coded vibrational mode assignments for both sets of radical products are shown above each spectrum.

to p -MeOPhS(\tilde{X}) radicals in their $v = 0$, $v_{6a} = 1, 2$, and $v_{18b} = 1$ levels; the p -MeOPhS(\tilde{A}) products show a similar distribution (except for no recognizable $v_{6a} = 2$ feature). Data acquired at $\lambda_{\text{phot}} = 300.0$ nm (Figure 9b) displays additional peaks assigned to $v_{9b} = 1$ in both the \tilde{X} and \tilde{A} state radicals. v_{9b} is an in-plane ring stretch motion coupled to the O–CH₃ bond wag. Arguments similar to those used for p -CH₃PhSH and p -FPhSH suggest that 300 nm excitation populates a resonance involving $v_{9b} = 1$ in the $1^1\pi\pi^*$ state.

Excitation to $\lambda_{\text{phot}} = 297.5$ nm (Figure 9c) reveals population of a progression in ν_{6a} (up to 4 quanta in p -MeOPhS(\tilde{X}) and up to 3 quanta in the \tilde{A} state products). The internal energy of the $1^1\pi\pi^*$ state molecules prepared at 297.5 nm is ~ 830 cm⁻¹, while $\tilde{\nu}_{6a}$ in the \tilde{X} state radical is 369 cm⁻¹. Neither the energetics, nor the observation of a progression (rather than one dominant additional peak in the E_{int} spectrum) matches the behavior found with PhSH⁶ and the other p -YPhSH molecules investigated in this work, where Franck–Condon excitation of a spectator mode in the $1^1\pi\pi^*$ state is seen to favor population of that same vibration in the radical product. This different form of energy disposal in the p -MeOPhS products extends to shorter wavelengths (Figure 9d,e). The latter spectrum shows the progression in ν_{6a} stretching up to 6 quanta at $\lambda_{\text{phot}} = 280.0$ nm and a near-Gaussian envelope associated with \tilde{X} state products extending to yet higher E_{int} . A progression in product mode ν_{6a} is specific to p -MeOPhSH photolysis and can be understood by recognizing that the nuclear motion associated with ν_{6a} is predicted to have more quinoidal character in the radical, i.e., the lengths of the C–C bonds parallel to the C–O bond are shorter than in the other p -YPhS radicals. This is analogous to the geometry change accompanying the $1^1\pi\pi^* \leftarrow S_0$ excitation in phenol.⁴⁶ We anticipate similar changes in the degree of quinoidal character upon $\pi^* \leftarrow \pi$ excitation in p -MeOPhSH (due to the strong electron donating character of the MeO group) and assume that FC activity in this mode underlies the observed progression in fragment mode ν_{6a} following S–H bond fission. Thus, although S–H bond cleavage is clearly a dominant dissociation pathway in p -MeOPhSH at these excitation wavelengths, the 2p_x O lone pair on the other side of the ring still makes a substantial contribution to the electronic structure (see HOMO in Figure 2h) of the molecule.

E_{int} spectra obtained at yet shorter photolysis wavelengths (275.0 and 270.0 nm, see Supplementary Figures S7a,b) show similar pairs of quasi-Gaussian envelopes peaking progressively further from 0 cm⁻¹, but no discernible structure in either product channel. At $\lambda_{\text{phot}} = 265.0$ nm (Figure 9f), however, we see an obvious step change in the E_{int} spectra, toward formation of radical products in low vibrational quantum states. This change in energy disposal coincides with the onset of a new feature in the UV absorption spectrum (recall Figure 3c) and mimics behavior exhibited by p -CH₃PhSH and p -FPhSH once the $1^1\pi\sigma^*$ state can be accessed directly. Indeed, the dynamics appears to favor the same subset of product vibrational states (see Figures 9f,g and S8) as in the corresponding photolyses of PhSH,⁶ p -CH₃PhSH, and p -FPhSH, but most of the products at these excitation wavelengths are \tilde{A} state p -MeOPhS radicals.

3.4.4. Recoil Anisotropy. $\beta(\text{TKER})$ was determined for each p -YPhSH molecule at many different photolysis wavelengths. Figure 10 displays illustrative plots for the photolysis of p -CH₃PhSH at (a–c) $\lambda_{\text{phot}} = 286.2$ nm and (d–f) 260.0 nm with ϵ_{phot} aligned at $\theta =$ (a,d) 90° and (b,e) 0°, with panels c and f showing $\beta(\text{TKER})$. The $\beta(\text{TKER})$ plot in Figure 10c is representative of data acquired for p -CH₃PhSH in the wavelength range $295 \geq \lambda_{\text{phot}} \geq 271$ nm, excitation energies that populate $1^1\pi\pi^*$ levels. The structured regions display preferential parallel recoil anisotropy. The anisotropy parameter associated with the peak at TKER_{max} , $\beta(\text{TKER}_{\text{max}})$, is $\sim +0.5$ and, as Figure 11 shows, is relatively invariant across the range $295 \geq \lambda_{\text{phot}} > 271$ nm. $\beta(\text{TKER}_{\text{max}})$ switches sign once the $1^1\pi\sigma^*$ state can be excited directly, as illustrated for the case of p -CH₃PhSH at $\lambda_{\text{phot}} = 260$ nm (Figures 10d–f). $\beta(\text{TKER}_{\text{max}})$ in

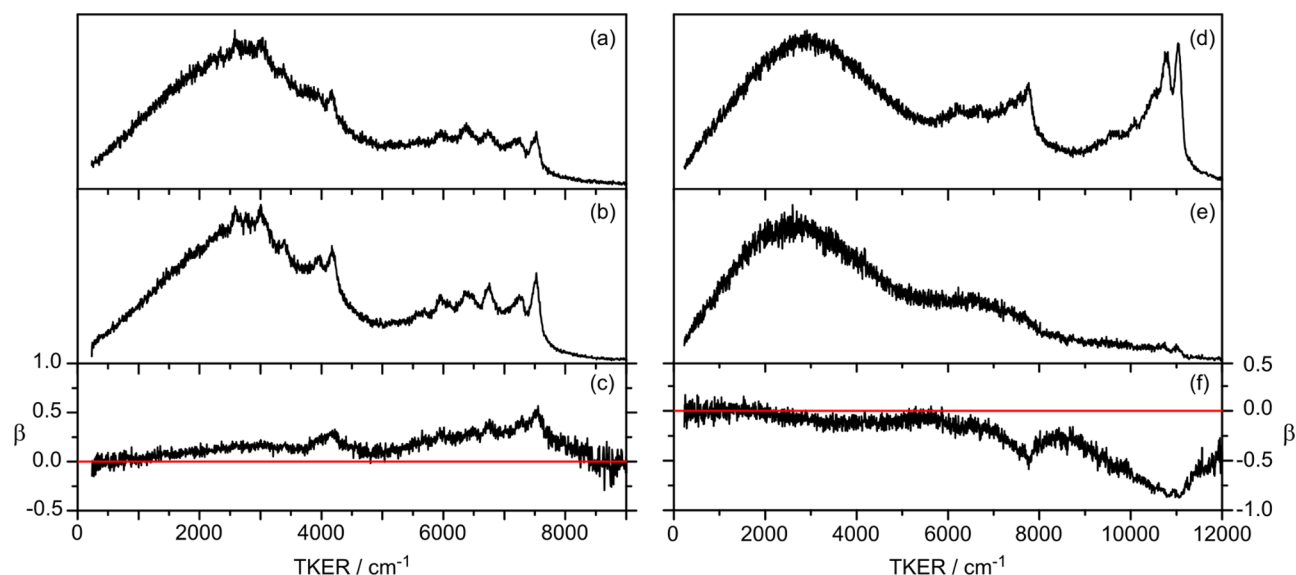


Figure 10. TKER spectra of the H + *p*-CH₃PhS products from photolysis of *p*-CH₃PhSH at $\lambda_{\text{phot}} = 286.2$ nm recorded at $\theta =$ (a) 90 and (b) 0°. The resulting recoil anisotropy parameter $\beta(\text{TKER})$ is shown in panel c. Panels d–f show the corresponding data recorded at $\lambda_{\text{phot}} = 260.0$ nm.

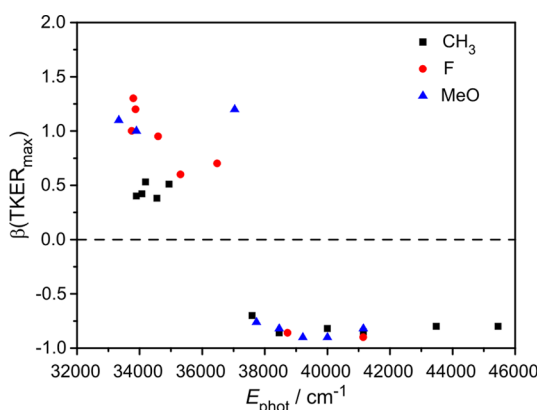


Figure 11. Recoil anisotropy of the H + *p*-YPhS products appearing at TKER_{max} , $\beta(\text{TKER}_{\text{max}})$, plotted as a function of photolysis energy, for all three *p*-YPhSH molecules.

this case is ~ -0.8 , a value that changes little across the range $271 \text{ nm} > \lambda_{\text{phot}} \geq 243 \text{ nm}$ (see Figure 11). The sign of $\beta(\text{TKER})$ measured at the longer excitation wavelengths, where photon absorption populates vibrational levels of the $1^1\pi\pi^*$ state, implies that the H atoms arising from S–H bond fission recoil preferentially parallel to the parent TDM. Such an observation accords with the EOM-CCSD/aug-cc-pVTZ calculations, which show the $1^1\pi\pi^* \leftarrow S_0$ TDM aligned roughly parallel to the S–H bond (see Figure 1).⁴⁹ At shorter wavelengths, where the $1^1\pi\sigma^*$ state is excited directly, the $\beta(\text{TKER}_{\text{max}})$ value tends to the limiting value of -1 , indicating a marked propensity for the H atom products to recoil perpendicular to the TDM. This, too, is consistent with the EOM-CCSD/aug-cc-pVTZ calculations, which show that the $1^1\pi\sigma^* \leftarrow S_0$ TDM lies perpendicular to the ring plane and the S–H bond; prompt fission of this bond should therefore eject H atoms at $\sim 90^\circ$ to ϵ_{phot} .

As Figure 11 shows, the fast H atom products from photolysis of *p*-FPhSH and *p*-MeOPhSH exhibit similar wavelength dependent trends in $\beta(\text{TKER}_{\text{max}})$. Sample $\beta(\text{TKER})$ plots following photolysis of both molecules are displayed in Figures S9–S12 in the Supporting Information.

The $\beta(\text{TKER}_{\text{max}})$ values observed when exciting to the $1^1\pi\pi^*$ states of *p*-FPhSH and *p*-MeOPhSH are both larger ($\beta(\text{TKER}_{\text{max}}) \sim +1.2$) than in the case of *p*-CH₃PhSH. This might seem slightly counterintuitive, given the S_0 torsional potentials presented in Figure 2. The calculated minimum energy geometry of *p*-MeOPhSH has the S–H bond at $\phi = 90^\circ$, though the associated barrier to planarity in the S_0 state is small. If the S–H bond were to break at $\phi = 90^\circ$ following $1^1\pi\pi^* \leftarrow S_0$ excitation, the resulting β parameter should be negative, contrary to the experimental observation. The rationale for this observation is the planar minimum energy geometry of the $1^1\pi\pi^*$ excited states and the larger value of E_{barrier} (an order of magnitude larger than in the S_0 state), which encourages the S–H group to move into the ring plane prior to bond fission, thereby yielding the observed preferential parallel H atom recoil anisotropy. Similar arguments must apply following $1^1\pi\pi^* \leftarrow S_0$ excitation in *p*-FPhSH. The calculated S_0 torsional potential in this case is very shallow, and it is reasonable to conclude that the dissociation geometry will again be largely determined by the minimum energy geometry of the $1^1\pi\pi^*$ state. Turning now to the $1^1\pi\sigma^* \leftarrow S_0$ excitations, analogous arguments must again hold for *p*-FPhSH and *p*-MeOPhSH, given the torsional PECs (recall Figure 2), which, in the vFC region, will drive the molecules toward planar excited state geometries and ensure that most H atoms recoil in the plane of the ring and thus perpendicular to ϵ_{phot} irrespective of whether the TDM vector is aligned along the x (i.e., out of the plane) or z axis as predicted for *p*-MeOPhSH (recall section 3.1).

The foregoing discussion does not account for the lower $\beta(\text{TKER}_{\text{max}})$ value observed following $1^1\pi\pi^* \leftarrow S_0$ excitation of *p*-CH₃PhSH, cf. *p*-FPhSH and *p*-MeOPhSH. Verifying any of the more likely explanations (dissociation on a longer time scale, allowing some rotational dephasing prior to S–H bond cleavage, for example) would require better knowledge of the PES surrounding the $1^1\pi\pi^*/1^1\pi\sigma^*$ CI than is currently available. Our most plausible rationale requires us to conclude that τ_{SH} is the principal coupling mode at this CI – see later discussion in section 3.4.5. The $1^1\pi\pi^*$ and S_0 states of *p*-CH₃PhSH both have planar equilibrium geometries (recall

Figure 2b), and our FC calculations (Supplementary Figure S2d) predict that the S–H bond in the photoexcited $1^1\pi\pi^*$ molecules will sample a relatively narrow range of dihedral angles around $\phi = 0^\circ$. The minimum energy configuration for the S_0 state of *p*-MeOPhSH, in contrast, has the S–H bond orthogonal to the ring plane. $1^1\pi\pi^* \leftarrow S_0$ excitation in this case will excite larger amplitude motion in τ_{SH} (see Supplementary Figure S2f), thereby facilitating coupling at the $1^1\pi\pi^*/1^1\pi\sigma^*$ CI and enabling faster predissociation. In this scenario, the larger $\beta(\text{TKER}_{\text{max}})$ value determined following $1^1\pi\pi^* \leftarrow S_0$ excitation in *p*-MeOPhSH (and *p*-FPhSH) thus reflects a shorter excited state lifetime. The apparent diffuseness of the UV absorption spectrum of *p*-MeOPhSH (Figure 3c) provides further circumstantial evidence for increased lifetime broadening in this molecule, though we recognize that this spectrum is also likely to contain the greatest amount of (unresolved) torsional fine structure (see Supplementary Figure S2f). This aside, the most striking aspect of the data shown in Figure 11 is the correlation between the $\beta(\text{TKER}_{\text{max}})$ values measured at a given photolysis wavelength for all three molecules, particularly when exciting the $1^1\pi\sigma^*$ state, which surely points to a common underlying dissociation mechanism.

3.4.5. Coupling at Conical Intersections. **3.4.5.1. $1^1\pi\pi^*/1^1\pi\sigma^*$ CI.** O–H bond fission in phenol following excitation to vibrational levels of the $1^1\pi\pi^*$ state occurs by H atom tunneling under the lower diabats of the $1^1\pi\pi^*/1^1\pi\sigma^*$ CI.^{18,19} Time-resolved pump–probe studies confirm the nanosecond time scale of this process in the gas⁵⁰ and solution phases.¹¹ The relative energies and shapes of the $1^1\pi\pi^*$ and $1^1\pi\sigma^*$ potentials in PhSH (and *p*-YPhSH) suggests that tunneling is likely to play a similarly key role in the S–H bond fission following excitation to the $1^1\pi\pi^*$ state. The energetic barrier under the $1^1\pi\pi^*/1^1\pi\sigma^*$ CI is much smaller, however (~ 0.12 eV in PhSH, cf., 0.83 eV for PhOH¹⁹ at the same level of ab initio theory), and comparable to the zero-point energy of the S–H stretch motion in the $1^1\pi\pi^*$ state. Thus, the H atom tunneling probabilities in PhSH and substituted thiophenols will be orders of magnitude larger. The lack of any sharp resonances in the electronic absorption spectra, our inability to induce resonance enhanced two photon ionization (despite a sufficiently low ionization potential⁵¹) and the lack of any discernible fluorescence,¹⁰ all support the expectation that the $1^1\pi\pi^*$ states of PhSH (and *p*-YPhSH) are very short-lived. The observation of fast H atoms, with recoil anisotropy appropriate for initial excitation to the $1^1\pi\pi^*$ state, and the deduction that Franck–Condon active skeletal vibrational motions in the photoexcited molecule map through into the radical products are also consistent with S–H bond fission by tunneling under the $1^1\pi\pi^*/1^1\pi\sigma^*$ CI. Previous D Rydberg atom PTS studies of PhSD photolysis reported broadly similar structured TKER spectra when exciting at the $1^1\pi\pi^* \leftarrow S_0$ origin,⁶ implying that the barrier to dissociation is insufficient to prevent the S–D bond fission process, although the experiments were not able to quantify the extent of any reduction in tunneling probability.

The vibrational energy disposal in the radical products is another point of distinction between phenol and the thiophenols. In the latter, we assign the TKER_{max} peaks to formation of $v = 0$ radical products, irrespective of whether the initial photoexcitation is to the $1^1\pi\pi^*$ and $1^1\pi\sigma^*$ state. Such analysis returns a self-consistent S–H bond strength for any given *p*-YPhSH molecule, in contrast to previous observations with phenol, where initial excitation to the $1^1\pi\pi^*$ state, tunneling under the $1^1\pi\pi^*/1^1\pi\sigma^*$ CI, and subsequent

dissociation on the $1^1\pi\sigma^*$ PES results in $\text{PhO}(\tilde{X})$ radicals carrying excitation in $\nu_{16a} = 1, 3$, etc. (i.e., odd quantum numbers only).¹² The observation of a short progression in ν_{16a} in the $\text{PhO}(\tilde{X})$ products is understandable on FC grounds (the wavenumber of the ν_{16a} mode halves upon $1^1\pi\pi^* \leftarrow S_0$ excitation and then returns to a value similar to that in the S_0 state as it evolves from the $1^1\pi\pi^*$ state to the $\text{PhO}(\tilde{X})$ radical),¹⁹ while the specific population of levels with $\nu_{16a} = \text{odd}$ has been rationalized by considering the $1^1\pi\pi^* \rightarrow 1^1\pi\sigma^*$ tunneling step in the G_4 permutation point group (isomorphic with C_{2v}).¹⁹ Viewed in this way, the initial and final states have 1B_2 and 1B_1 symmetry, respectively, and nonadiabatic coupling between the states thus requires a nuclear motion of a_2 symmetry. ν_{16a} is the lowest frequency motion of the appropriate symmetry (none of the modes associated with the O–H group have a_2 symmetry) and 2-D wavepacket calculations of the $1^1\pi\pi^* \rightarrow 1^1\pi\sigma^*$ tunneling process with q_{16a} as the coupling mode successfully reproduce the observed propensity for forming $\text{PhO}(\tilde{X})$ products with $\nu_{16a} = \text{odd}$ only.¹⁹

In the first instance, we might expect that similar symmetry arguments would apply in the case of PhSH and the symmetrically substituted *p*-YPhSH molecules, but we recognize two important differences between PhSH and PhOH, which could account for the observed differences in product vibrational energy disposal. As noted previously (Table 1), the barrier to S–H torsional motion in the S_0 state is small: $< 270 \text{ cm}^{-1}$ in all of the *p*-YPhSH molecules, cf., the corresponding barrier in PhOH, $E_{\text{barrier}} \sim 1215 \text{ cm}^{-1}$ (ref 52). Thus, the initial S_0 molecules span a wider spread of ϕ than in PhOH, which will be projected into the $1^1\pi\pi^*$ state upon photoexcitation (and amplified further in the case that $Y = \text{F}$ or MeO). Second, the barrier under the lower diabats of the $1^1\pi\pi^*/1^1\pi\sigma^*$ CI in the R_{S-H} coordinate is ~ 7 times smaller in PhSH than the corresponding barrier in R_{O-H} in phenol, and thus presents little impediment to dissociation. Thus, we arrive at a picture where activity in τ_{SH} induced in the photoexcitation step is sufficient to mediate the $1^1\pi\pi^*/1^1\pi\sigma^*$ coupling, and the $1^1\pi\pi^*$ state lifetime is just too short to allow nuclear motion in other potential coupling modes (e.g., ν_{16a}) to develop; the dynamics should thus be viewed in the C_s point group where τ_{SH} has the appropriate symmetry to couple the relevant PESs. Recent wavepacket calculations for PhSH, which return $1^1\pi\pi^*$ state lifetimes (with respect to H atom tunneling) of $\sim 1 \text{ ps}$,¹⁷ lend support to this hypothesis, particularly when considered in light of the present electronic structure calculations (that include aug-functions on C and H atoms), which return a substantially ($\sim 50\%$) smaller barrier height under the lower diabats of the $1^1\pi\pi^*/1^1\pi\sigma^*$ CI, that would inevitably translate into even faster tunneling rates.

3.4.5.2. $1^1\pi\sigma^*/S_0$ CI. All of the present data supports the view that coupling at the $1^1\pi\sigma^*/S_0$ CI is also mediated by S–H torsional motion. Such a conclusion accords with the predictions of Domcke and co-workers regarding coupling at the $1^1\pi\sigma^*/S_0$ CI in both PhOH³⁸ and PhSH,¹⁷ with the findings of Lim et al.,⁵ and with the independent determination of ΔE ($\text{PhS}(\tilde{A}-\tilde{X})$) by the Neumark group,¹⁶ and corrects the interpretation offered in our initial study of PhSH photolysis.⁶

Understanding the basis for branching into the *p*-YPhS(\tilde{A}) + H product channel in the present study allows us to gain a better insight as to why the reported photodissociation dynamics of PhOH give very small, if not negligible, yields of $\text{PhO}(\tilde{A})$ radicals.¹³ Important factors include, first, the

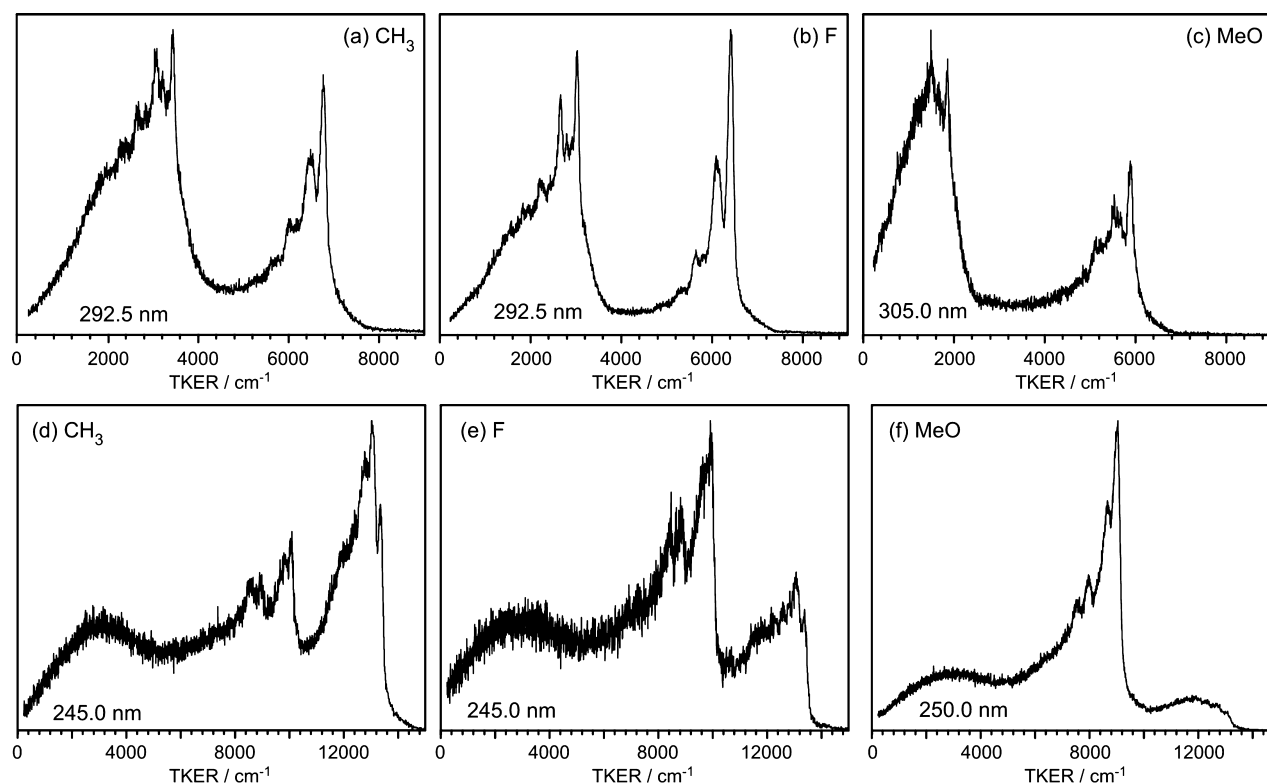


Figure 12. Comparison of the TKER spectra of the H + *p*-YPhS products formed by photolysis of each *p*-YPhSH molecule at its respective $1^1\pi\pi^*$ – S_0 origin (panels a–c) and when exciting directly to the $1^1\pi\sigma^*$ state (panels d–f).

(relative) rigidity of the S_0 and $1^1\pi\pi^*$ torsional potentials,⁵² which are greater in PhOH and will thus result in less amplitude at $\phi \neq 0^\circ$ and thence less adiabatic behavior at the $1^1\pi\sigma^*/S_0$ CI. Second, the topography of the adiabatic PES between this CI and the dissociation limit is steeper because of the larger energy splitting in the PhO radical ($\Delta E(\tilde{A}-\tilde{X}) = 7990 \text{ cm}^{-1}$), disfavoring PhO(\tilde{A}) products on Landau–Zener grounds.

3.4.6. \tilde{X}/\tilde{A} Branching Fractions in *p*-YPhS Radicals. Figure 12 displays TKER spectra obtained at two representative photolysis wavelengths for each of the three *p*-YPhSH molecules studied in this work. Figure 12a–c were acquired at wavelengths resonant with the first maximum in the respective absorption spectra (Figure 3a–c), i.e., at the respective $1^1\pi\pi^*$ – S_0 origins. H + *p*-YPhS(\tilde{X}) and H + *p*-YPhS(\tilde{A}) products are formed in all cases. Figure 12d–f show TKER spectra recorded at $\lambda_{\text{phot}} \sim 245 \text{ nm}$ and are representative of data obtained when the $1^1\pi\sigma^*$ state is directly excited. In line with the data of Kim and co-workers,⁵ we find that the relative yield of *p*-YPhS(\tilde{A}) fragments increases substantially along the series $Y = \text{CH}_3 < \text{F} < \text{MeO}$.

We first consider the data obtained following excitation of the $1^1\pi\pi^*$ state. A quantitative analysis was attempted by fitting TKER spectra recorded at several different wavelengths to three functions: a Gumbel function, as has been used previously to model TKER signal arising from unimolecular decay of highly vibrationally excited molecules on the S_0 PES,⁵³ and two extreme functions for the H + *p*-YPhS(\tilde{X}) and (\tilde{A}) products (see Supporting Information for further details and representative fits in Figures S13–S15). Numerical integration under the fitted areas associated with \tilde{X} and \tilde{A} state radical products arising from dissociation on the excited state PES then enabled calculation of the \tilde{X}/\tilde{A} branching ratio, Γ . The results from such

analyses are presented in Figure 13. Excitations to $1^1\pi\pi^*$ levels in both *p*-CH₃PhSH and *p*-FPhSH yield branching ratios in the

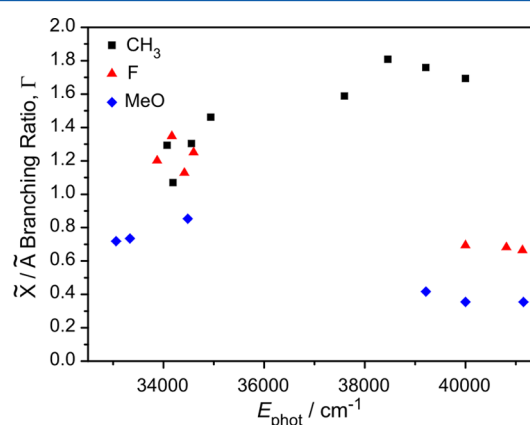


Figure 13. Photolysis energy dependence of the \tilde{X}/\tilde{A} branching ratio, Γ , in the *p*-YPhS products from *p*-CH₃PhSH, *p*-FPhSH, and *p*-MeOPhSH.

range $1.5 > \Gamma > 1$ (i.e., show a small preference for forming \tilde{X} state products), whereas the corresponding excitation in *p*-MeOPhSH returns $0.5 < \Gamma < 0.9$. These findings chime with the wavepacket calculations of Venkatesan et al.,¹⁷ and the Y dependence of the ground state torsional potentials (Figure 2). The former reveal a preference for \tilde{A} state products when exciting $1^1\pi\pi^*$ levels of PhSH carrying two quanta of τ_{SH} ,¹⁷ while the torsional PECs (and FC simulations) imply that the propensity for populating highly excited torsional levels in the $1^1\pi\pi^*$ state is greatest in *p*-MeOPhSH (see Supplementary Figure S2f), and least in the cases of PhSH and *p*-CH₃PhSH.

Table 3. Summary of Key Energetic Quantities (in cm^{-1}) Derived in This Study: Absorption Onsets from PHOFEX and UV Absorption Spectra, $1^1\pi\sigma^*-1^1\pi\pi^*$ Energy Splittings from the Evident Step Change in the Product Vibrational Energy Disposal in the Measured TKER Spectra, S–H Bond Strengths (To Both \tilde{X} and \tilde{A} Product State Asymptotes), and the Energy Splitting so Derived between These Two States of the Radical; Values for PhSH Are Tabulated Also, after Appropriate Correction of the Assignments Offered in the Earlier HRA-PTS Study⁶ (See Text for Further Details)

Y	$\Delta E(1^1\pi\pi^*-S_0)$	$\Delta E(1^1\pi\sigma^*-1^1\pi\pi^*)$	$D_0(p\text{-YPhS}(\tilde{X})-\text{H})$	$D_0(p\text{-YPhS}(\tilde{A})-\text{H})$	$\Delta E(\tilde{A}-\tilde{X})$
H	34 480	1880	28 030	31 590	2960
CH_3	34 190	2710	27 430	30 750	3320
F	33 880	3920	27 420	30 840	3420
MeO	32 790	4950	26 860	30 860	4000

However, the recoil anisotropy measurements (Figure 11) show that the H atom products recoil preferentially parallel to ϵ_{phot} ($\beta(\text{TKER}_{\text{max}}) > 0$), and thus to the parent $1^1\pi\pi^*-S_0$ TDM, which, as Figure 1 showed, lies along the y axis (i.e., in the ring plane).

Thus, the following overall picture emerges: photoexcitation creates $p\text{-YPhS}(1^1\pi\pi^*)$ molecules with a (Y-dependent) spread of geometries over ϕ (as dictated by the distribution in S_0), which couple efficiently to the dissociative $1^1\pi\sigma^*$ PES. The topographies of the excited state potentials are such that any intramolecular vibrational redistribution (IVR), prior to tunneling from the $1^1\pi\pi^*$ state (or during S–H bond extension on the $1^1\pi\sigma^*$ PES), will encourage relaxation toward planarity. The branching between the \tilde{X} and \tilde{A} states of the radical products is determined in the vicinity of the $1^1\pi\sigma^*/S_0$ CI. Dissociating molecules with $\phi \sim 0^\circ$ are drawn into this CI and follow the diabatic path to \tilde{X} state products, whereas molecules evolving with less planar geometries avoid this CI and follow the adiabatic path to $p\text{-YPhS}(\tilde{A})$ state radical products. Γ must therefore reflect a convolution of the spread of torsional geometries prepared in the $1^1\pi\pi^*$ state, any subsequent damping in ϕ as the S–H bond extends, and the detailed topography of the $1^1\pi\sigma^*/S_0$ CI in each of the $p\text{-YPhS}$ molecules.

Γ shows a greater Y dependence when exciting directly to the $1^1\pi\sigma^*$ state, as illustrated in Figures 12d–f and 13. We start by considering the extreme cases of $Y = \text{CH}_3$ and MeO. In the former, $p\text{-CH}_3\text{PhS}(\tilde{X})$ products dominate ($\Gamma > 1.5$), while, in the latter, the converse is true; $p\text{-MeOPhS}(\tilde{A})$ products dominate, and $\Gamma < 0.4$. These contrasting behaviors are understandable in light of the previous discussion. The electronic structure calculations predict planar minimum energy geometries for both the S_0 and $1^1\pi\sigma^*$ states of $p\text{-CH}_3\text{PhSH}$. Franck–Condon considerations suggest little torsional excitation in the excited molecules. The dissociating molecules will span a range of geometries peaked around $\phi = 0^\circ$, and the substantial fraction that are sufficiently close to planar when moving through the vicinity of the $1^1\pi\sigma^*/S_0$ CI follow the diabatic path to $p\text{-CH}_3\text{PhS}(\tilde{X})$ products, and the large value of Γ follows naturally. $p\text{-MeOPhSH}$ represents the other extreme; the minimum energy geometry of the $1^1\pi\sigma^*$ state is again planar, but the CCSD(T)(F12*) calculations predict $\phi_{\text{min}} = 90^\circ$ in the S_0 state. Vertical excitation in this case will project molecules onto the $1^1\pi\sigma^*$ PES at nonplanar geometries. The topography of the $1^1\pi\sigma^*$ PES ensures that S–H bond extension will be accompanied by some SH torsional motion; the experimental data indicates that most of the dissociating flux avoids the $1^1\pi\sigma^*/S_0$ CI and evolves to $\text{H} + p\text{-MeOPhS}(\tilde{A})$ products, in accord with the earlier results and discussion of Kim and co-workers.⁵ $1^1\pi\sigma^*-S_0$ excitation of $p\text{-FPhSH}$ also results in preferential formation of \tilde{A} state products ($\Gamma < 0.7$),

but the bias is less marked than in the case of $p\text{-MeOPhSH}$. Once again, such a trend can be qualitatively rationalized in light of the relevant potentials (Figure 2e,f), which suggest that the distribution of photoprepared $1^1\pi\sigma^*$ molecules will be centered around planar geometries but span a considerably wider range of ϕ than in the case of $p\text{-CH}_3\text{PhSH}$ or PhSH.

3.4.7. S–H Bond Strengths and the \tilde{A} – \tilde{X} State Energy Splitting in the $p\text{-YPhS}$ Radicals. The present data allows us to examine the effects of *para*-substitution and its Y dependence via several metrics: the S–H bond strength, the energy splitting between the \tilde{A} and \tilde{X} states of the $p\text{-YPhS}$ radical, the $1^1\pi\pi^*-S_0$ term value, and the separation of the $1^1\pi\sigma^*$ and $1^1\pi\pi^*$ states in the vFC region (Table 3). The electron donating ability of the Y substituents increases in the order: $\text{H} < \text{CH}_3 < \text{F} < \text{MeO}$. The S–H bond strength decreases incrementally, in the same order, by $\sim 1200 \text{ cm}^{-1}$, reflecting the enhanced stabilization of the ground state radical (which has a $p_x\pi$ hole) by an electron donating substituent. The SOMO in the \tilde{A} state radical is a $p_y\sigma$ orbital and thus orthogonal to the π -system and rather immune to changes in *para*-substituent, as evidenced by the near constancy of $D_0(p\text{-YPhS}(\tilde{A})-\text{H})$. This rationale also accounts for the observed increase in the energetic separation of the \tilde{A} and \tilde{X} states of the radical. The stabilization of the \tilde{X} state radical by *para*-substitution with an electron donating group leads to a concomitant lowering of the $1^1\pi\sigma^*$ vertical excitation energy. Yet such substitution is also seen to increase the vertical energy separation between the $1^1\pi\sigma^*$ and $1^1\pi\pi^*$ states. This is because *para*-substitution causes a red shift in the onset of $1^1\pi\pi^* \leftarrow S_0$ absorption, which is greatest in the case of a strong π donor, like MeO, where the additional π -density acquired by conjugating with the $\text{O}(2p\pi)$ lone pair destabilizes the HOMO (π), but seemingly has relatively little effect on the LUMO (π^*). As noted previously, the progressive reduction in the height of the torsional barrier in the S_0 states of these thiophenols is another manifestation of the destabilization of the HOMO by electron donating substituents in the *para*-position, which culminates in the finding that the S–H bond prefers to sit out of the ring plane in the S_0 state of $p\text{-MeOPhSH}$.

4. CONCLUSIONS

The dynamics of S–H bond fission following photoexcitation of three *para*-substituted thiophenols has been studied at many different UV excitation wavelengths using H (Rydberg) atom photofragment translational spectroscopy in combination with high-level CCSD(T)(F12*), EOM-CCSD, and CASPT2 calculations. We demonstrate that the branching between ground (\tilde{X}) and excited (\tilde{A}) state $p\text{-YPhS}$ radical products can be controlled by judicious choice of the Y substituent and the excitation wavelength, i.e., by the choice of excited state populated by photon absorption. The present findings are in

broad agreement with conclusions reached in earlier ion imaging studies (at just one photolysis wavelength, $\lambda_{\text{phot}} = 243.1$ nm),⁵ but the many additional wavelengths investigated here and the availability of higher level ab initio torsional potentials for the various ground and excited states reveal a greater richness to the fragmentation dynamics of these molecules than hitherto recognized.

The electronic branching in the products is dictated by the way molecules evolving on the $1^1\pi\sigma^*$ PES sample the $1^1\pi\sigma^*/S_0$ CI at extended $R_{\text{S-H}}$ bond lengths.^{3–7,9} Molecules approaching with near planar geometries (i.e., with $\phi \sim 0^\circ$) can pass through this CI and evolve to the diabatic (\tilde{X} state radical) products, whereas molecules approaching with ϕ away from zero tend to follow the adiabatic path and correlate to \tilde{A} state radicals. Excitation at $\lambda_{\text{phot}} < 265$ nm results in direct population of the $1^1\pi\sigma^*$ state, and the \tilde{X}/\tilde{A} branching ratio reflects the distribution of parent geometries (over ϕ) prior to excitation. In the case of PhSH or *p*-CH₃PhSH, $\phi_{\text{min}} \sim 0^\circ$ and \tilde{X} state products dominate ($\Gamma > 1.5$), whereas for *p*-MeOPhSH, $\phi_{\text{min}} \sim 90^\circ$ and the majority products are \tilde{A} state radicals ($\Gamma < 0.4$). *p*-FPhSH shows intermediate behavior, consistent with the present electronic structure calculations, which predict a very low barrier to torsional motion in the S_0 state. Excitation at $\lambda_{\text{phot}} > 265$ nm in all cases populates levels of the $1^1\pi\pi^*$ state, which are diabatically bound with respect to S–H bond fission but, as in phenol,¹⁹ can predissociate by tunneling through the barrier under the $1^1\pi\pi^*/1^1\pi\sigma^*$ CI. The calculated height of this barrier is ~ 7 times smaller than that in phenol¹⁹ and comparable to the ZPE in the S–H stretch coordinate. Experimental support for the proposed efficient tunneling process comes from the observed anisotropy of the recoiling H atom products and the vibrational energy disposal in the radical products. The latter is rationalized on the grounds that coupling at the $1^1\pi\pi^*/1^1\pi\sigma^*$ CI is mediated by τ_{SH} and that the excited state lifetime is too short to allow the development of other possible coupling modes (e.g., ring skeletal motions such as ν_{16a} that promote coupling at the analogous CI in phenol.¹⁹) Nonetheless, the sequence of $1^1\pi\pi^* \leftarrow S_0$ excitation, followed by IVR and damping of torsional motion on the $1^1\pi\pi^*$ PES prior to passage through the $1^1\pi\pi^*/1^1\pi\sigma^*$ CI region and subsequent evolution on the $1^1\pi\sigma^*$ PES toward the region of the $1^1\pi\sigma^*/S_0$ CI, is seen to result in less extreme \tilde{X}/\tilde{A} branching ratios (e.g., $1.5 > \Gamma > 1$ for *p*-CH₃PhSH, and $0.9 > \Gamma > 0.5$ for *p*-MeOPhSH) than in the case of direct $1^1\pi\sigma^* \leftarrow S_0$ excitation. Thus, simply tuning the excitation wavelength has a marked effect on the \tilde{X}/\tilde{A} branching in the *p*-YPhS radicals. The vibrational energy disposals in the \tilde{X} and \tilde{A} state products from photolysis of any given *p*-YPhSH molecule at any given wavelength are very similar, reinforcing the view that these skeletal motions are established early in the dissociation process, well before reaching the $1^1\pi\sigma^*/S_0$ CI at $R_{\text{S-H}} \sim 2.5$ Å.

The comprehensive description of the UV photodissociation dynamics of the *p*-YPhSH molecules reported in this study rests on a wealth of high-resolution experimental data and companion high-level CCSD(T)(F12*), EOM-CCSD, and CASPT2 calculations. The present analysis has also enabled a reappraisal of the energy disposal in the products arising from UV photodissociation of bare thiophenol, yielding a picture that is now fully consistent with the earlier theoretical studies by Domcke and co-workers¹⁷ and with the energetics of the PhS radical derived from photodetachment studies of the thiophenoxide anion.¹⁶

■ ASSOCIATED CONTENT

§ Supporting Information

(i) Details regarding the extraction of TKER-dependent β parameters from the measured data; (ii) a description of the zero-point energy calculations and of the effective torsional potentials, eigenvalues, and Franck–Condon factors; (iii) the additional (*p*-Y)PhS radical E_{int} spectra discussed in the text; (iv) a description of the way measured TKER spectra have been decomposed to allow estimation of Γ , the \tilde{X}/\tilde{A} product branching ratio; (v) lists of the calculated harmonic and anharmonic wavenumbers for the normal mode vibrations of the *p*-YPhS radicals ($Y = \text{CH}_3$, F, and MeO); and (vi) identifications of short-lived vibronic resonances within the $1^1\pi\pi^* \leftarrow S_0$ absorptions of *p*-CH₃PhSH and *p*-FPhSH as revealed by analysis of TKER spectra of the S–H bond fission products. This material is available free of charge via the Internet at <http://pubs.acs.org>.

■ AUTHOR INFORMATION

Corresponding Author

*Tel: +44 (117) 928 8312. Fax: +44 (117) 925 0612. E-mail: mike.ashfold@bris.ac.uk.

Present Addresses

[†]Department of Chemistry, University of California Berkeley, Berkeley, California 94720, United States.

[‡]Department of Physics and Astronomy, VU University, Faculty of Sciences, De Boelelaan 1081, NL-1081 HV Amsterdam, The Netherlands.

Notes

The authors declare no competing financial interest.

■ ACKNOWLEDGMENTS

We are grateful to EPSRC for the award of a programme grant EP/G00224X, and to Tom Zhang and Steve Bradforth at the University of Southern California for many useful discussions. We would like to also thank Adam Devine, Mike Nix, Jeremy Harvey, Keith Rosser, and James Smith for their contributions to this work. D.P.T. and M.N.R.A. are grateful to the Royal Society for the awards of, respectively, a University Research Fellowship and a Leverhulme Trust Senior Research Fellowship.

■ REFERENCES

- (1) Sobolewski, A. L.; Domcke, W.; Dedonder-Lardeux, C.; Jouvet, C. *Phys. Chem. Chem. Phys.* **2002**, *4*, 1093–1100.
- (2) Ashfold, M. N. R.; King, G. A.; Murdock, D.; Nix, M. G. D.; Oliver, T. A. A.; Sage, A. G. *Phys. Chem. Chem. Phys.* **2010**, *12*, 1218–1238.
- (3) Lim, J. S.; Lim, I. S.; Lee, K.-S.; Ahn, D.-S.; Lee, Y. S.; Kim, S. K. *Angew. Chem., Int. Ed.* **2006**, *45*, 6290–6293.
- (4) Lim, I. S.; Lim, J. S.; Lee, S. Y.; Kim, S. K. *J. Chem. Phys.* **2007**, *126*, 034306.
- (5) Lim, J. S.; Lee, Y. S.; Kim, S. K. *Angew. Chem., Int. Ed.* **2008**, *47*, 1853–1856.
- (6) Devine, A. L.; Nix, M. G. D.; Dixon, R. N.; Ashfold, M. N. R. *J. Phys. Chem. A* **2008**, *112*, 9563–9574.
- (7) Ashfold, M. N. R.; Devine, A. L.; Dixon, R. N.; King, G. A.; Nix, M. G. D.; Oliver, T. A. A. *Proc. Natl. Acad. Sci.* **2008**, *105*, 12701–12706.
- (8) Lim, J. S.; Choi, H.; Lim, I. S.; Park, S. B.; Lee, Y. S.; Kim, S. K. *J. Phys. Chem. A* **2009**, *113*, 10410–10416.
- (9) Oliver, T. A. A.; Zhang, Y.; Ashfold, M. N. R.; Bradforth, S. E. *Faraday Disc.* **2011**, *150*, 439–458.

- (10) Zhang, Y.; Oliver, T. A. A.; Ashfold, M. N. R.; Bradforth, S. E. To be submitted.
- (11) Zhang, Y.; Oliver, T. A. A.; Ashfold, M. N. R.; Bradforth, S. E. *Faraday Disc.* **2012**, *157*, 141–163.
- (12) Nix, M. G. D.; Devine, A. L.; Cronin, B.; Dixon, R. N.; Ashfold, M. N. R. *J. Chem. Phys.* **2006**, *125*, 133318.
- (13) King, G. A.; Oliver, T. A. A.; Nix, M. G. D.; Ashfold, M. N. R. *J. Phys. Chem. A* **2009**, *113*, 7984–7993.
- (14) Mulder, P.; Mozenon, O.; Lin, S.; Bernardes, C. E. S.; Minas da Pedade, M. E.; Santos, A. F. L. O. M.; Ribeiro da Silva, M. A. V.; DiLabio, G. A.; Korth, H.-G.; Ingold, K. U. *J. Phys. Chem. A* **2006**, *110*, 9949–9958.
- (15) Larsen, N. W.; Schulz, L. *J. Mol. Struct.* **2009**, *920*, 30–39.
- (16) Kim, J. B.; Yacovitch, T. I.; Hock, C.; Neumark, D. M. *Phys. Chem. Chem. Phys.* **2011**, *13*, 17378–17383.
- (17) Venkatesan, T. S.; Ramesh, S. G.; Lan, Z.; Domcke, W. *J. Chem. Phys.* **2012**, *136*, 174312.
- (18) Pino, G. A.; Olfdani, A. N.; Marceca, E.; Fujii, M.; Ishiucji, S.-I.; Miyazaki, M.; Broquier, M.; Dedonder, C.; Jouvet, C. *J. Chem. Phys.* **2010**, *133*, 124313.
- (19) Dixon, R. N.; Oliver, T. A. A.; Ashfold, M. N. R. *J. Chem. Phys.* **2011**, *134*, 194303.
- (20) Cronin, B.; Nix, M. G. D.; Qadiri, R. H.; Ashfold, M. N. R. *Phys. Chem. Chem. Phys.* **2004**, *6*, 5031–5041.
- (21) Hampel, C.; Peterson, K.; Werner, H.-J. *Chem. Phys. Lett.* **1992**, *190*, 1–12 and references therein.
- (22) El Azhary, A.; Rauhut, G.; Pulay, P.; Werner, H.-J. *J. Chem. Phys.* **1998**, *108*, 5185–5193.
- (23) Dunning, T. H., Jr. *J. Chem. Phys.* **1989**, *90*, 1007–1023.
- (24) Dunning, T. H., Jr.; Peterson, K. A.; Wilson, A. K. *J. Chem. Phys.* **2001**, *114*, 9244–9253.
- (25) Werner, H.-J.; Adler, T. B.; Manby, F. R. *J. Chem. Phys.* **2007**, *126*, 164102.
- (26) Hättig, C.; Tew, D. P.; Köhn, A. *J. Chem. Phys.* **2010**, *132*, 231102.
- (27) Adler, T. B.; Knizia, G.; Werner, H.-J. *J. Chem. Phys.* **2007**, *127*, 221106.
- (28) Korona, T.; Werner, H.-J. *J. Chem. Phys.* **2003**, *118*, 3006–3019.
- (29) Hellweg, A. *Chem. Phys. Lett.* **2009**, *475*, 198–201.
- (30) *Turbomole*, V6.3; University of Karlsruhe and Forschungszentrum Karlsruhe GmbH: Karlsruhe, Germany, 2011; available from <http://www.turbomole.com>.
- (31) Werner, H.-J.; Knowles, P. J. *J. Chem. Phys.* **1985**, *82*, 5053–5063. Knowles, P. J.; Werner, H.-J. *Chem. Phys. Lett.* **1985**, *115*, 259–267.
- (32) Werner, H.-J. *Mol. Phys.* **1996**, *89*, 645–661.
- (33) Celani, P.; Werner, H.-J. *J. Chem. Phys.* **2003**, *119*, 5044–5057.
- (34) Werner, H.-J.; Knowles, P. J.; Manby, F. R.; Schütz, M.; Celani, P.; Knizia, G.; Korona, T.; Lindh, R.; Mitrushenkov, A.; Rauhut, G.; Adler, T. B.; Amos, R. D.; et al. *MOLPRO*; University of Cardiff: Cardiff, U.K., 2010.
- (35) Frisch, M. J.; Trucks, G. W.; Schlegel, H. B.; Scuseria, G. E.; Robb, M. A.; Cheeseman, J. R.; Montgomery, J. A., Jr.; Vreven, T.; Kudin, K. N.; Burant, J. C.; et al. *Gaussian 03*, revision B.04; Gaussian Inc.: Wallingford, CT, 2003.
- (36) Krishnan, R.; Binkley, J. S.; Seeger, R.; Pople, J. A. *J. Chem. Phys.* **1980**, *72*, 650–654. McLean, A. D.; Chandler, G. S. *J. Chem. Phys.* **1980**, *72*, 5639–5648.
- (37) Lan, Z. G.; Domcke, W.; Vallet, V.; Sobolewski, A. L.; Mahapatra, S. *J. Chem. Phys.* **2005**, *122*, 224315.
- (38) Vieuxmaire, O. P. J.; Lan, Z.; Sobolewski, A. L.; Domcke, W. *J. Chem. Phys.* **2008**, *129*, 224307.
- (39) Reisler, H.; Krylov, A. I. *Int. Rev. Phys. Chem.* **2009**, *28*, 267–308.
- (40) Lee, T. J.; Scuseria, G. E. *Quantum Mechanical Electronic Structure Calculations with Chemical Accuracy*; Langhoff, S. R., Ed.; Kluwer Academic Publishers: Dordrecht, The Netherlands, 1995.
- (41) Larsen, N. W.; Nicolaisen, F. M. *J. Mol. Struct.* **1974**, *22*, 29–43.
- (42) Oliver, T. A. A.; King, G. A.; Nix, M. G. D.; Ashfold, M. N. R. *J. Phys. Chem. A* **2010**, *114*, 1338–1346.
- (43) Di Lonardo, G.; Zauli, C. *J. Chem. Soc. A* **1969**, 1305–1306.
- (44) Hollas, J. M. *Spectrochim. Acta* **1963**, *19*, 753–767.
- (45) Kimura, K.; Tsubomura, H.; Nagakura, S. *Bull. Chem. Soc. Jpn.* **1964**, *37*, 1336–1346.
- (46) Bist, H. D.; Brand, J. C. D.; Williams, D. R. *J. Mol. Spectrosc.* **1966**, *21*, 76–98; **1967**, *24*, 402–412; **1967**, *24*, 413–467.
- (47) Schick, C. P.; Weber, P. M. *J. Phys. Chem. A* **2001**, *105*, 3725–3734.
- (48) Wilson, E. B. *Phys. Rev.* **1934**, *45*, 706–714.
- (49) We recognize that torsion about the C–S bond is likely to degrade β from the limiting value (+2) that might be expected for prompt S–H bond fission following parallel excitation to a planar excited state (i.e., in the limit of axial recoil).
- (50) Roberts, G. M.; Chatterley, A. S.; Young, J. D.; Stavros, V. G. *J. Phys. Chem. Lett.* **2012**, *3*, 348–352.
- (51) Faulk, J. D.; Dunbar, R. C.; Lifshitz, C. *J. Am. Chem. Soc.* **1990**, *112*, 7893–7899.
- (52) Gerden, G.; Meerts, W. L.; Schmitt, M.; Kleinermaans, K. *J. Chem. Phys.* **1996**, *104*, 972–982.
- (53) Qadiri, R. H.; Feltham, E. J.; Nahler, N. H.; Garcia, R. P.; Ashfold, M. N. R. *J. Chem. Phys.* **2003**, *119*, 12842–12851.